Geochemistry, Geophysics, Geosystems

RESEARCH ARTICLE
10.1029/2020GC009539

Key Points:

- Zircon from a migmatitic pelitic granulite has variable ages, while Y, Th, U, Hf and HREE, Th/U and Eu/Eu* of zircon show systematic changes over time
- The granulite experienced high-temperature metamorphism, partial melting, and melt crystallization over ~20 Myr
- Intensive melting during burial triggered the exhumation of granulites and contributed to the formation of Himalayan leucogranites

Supporting Information:

Supporting Information may be found in the online version of this article.

Correspondence to:

Z. Zhang,
zzm2111@sina.com

Citation:

Ding, H., Zhang, Z., Kohn, M. J., & Gou, Z. (2021). Timescales of partial melting and melt crystallization in the eastern Himalayan orogen: Insights from zircon petrochronology. *Geochemistry, Geophysics, Geosystems*, *22*, e2020GC009539. https://doi.org/10.1029/2020GC009539

Received 11 NOV 2020
Accepted 19 MAR 2021

Timescales of Partial Melting and Melt Crystallization in the Eastern Himalayan Orogen: Insights From Zircon Petrochronology

Huixia Ding[1], Zeming Zhang[1,2], Matthew J. Kohn[3], and Zhengbin Gou[4]

[1]State Key Laboratory of Geological Processes and Mineral Resources, School of Earth Sciences and Resources, China University of Geosciences, Beijing, China, [2]Institute of Geology, Chinese Academy of Geological Sciences, Beijing, China, [3]Department of Geosciences, Boise State University, Boise, ID, USA, [4]Chengdu Center, China Geological Survey, Chengdu, China

Abstract Revealing the timescales of metamorphic and anatectic processes is central to our understanding of tectonic evolution of collisional orogens. High-temperature migmatites and leucogranites are well exposed in the Himalayan orogenic core, making it an ideal region to study the timing and duration of partial melting and melt crystallization of the orogen. Here, we report an integrated and comprehensive data set of petrography, U-Pb age, and trace element data for zircon from a pelitic granulite and associated leucosomes of the Greater Himalayan Sequence (GHS) in the Yadong area, eastern Himalaya. Zircon grains with complex internal structure retain variable ages ranging from 32 Ma to 13 Ma that correlate systematically with changes in the concentrations of Y, Th, U, Hf, Nb, Ta, and HREE, and ratios of Th/U, Eu/Eu*, and Nb/Ta. Combined with petrologic analysis, we conclude that the granulite witnessed high-temperature metamorphism, melting, and melt crystallization over ~20 Myr. Prograde, simultaneous increases in pressure and temperature and associated dehydration melting began at least by ~32 Ma and lasted until ~24 Ma. Subsequent quasi-isothermal decompression-melting occurred between ~22 and 19 Ma, and late melt crystallization spanned ~19 to 13 Ma. Large volumes of melt generated during prograde metamorphism could have triggered exhumation of GHS rocks, increasing melt fraction through a positive feedback between exhumation and melting. More comprehensive analysis of different rock types led to more complete and different interpretations for the timing of exhumation and melt crystallization in the Yadong-Sikkim region and might enable alternate interpretations elsewhere in the Himalayas.

1. Introduction

Melting drastically weakens rocks (e.g., Rosenberg & Handy, 2005; Sawyer et al., 2011) and thus is a key factor that controls the tectonic evolution of orogens (Beaumont et al., 2001, 2004; Jamieson et al., 2004; Rey et al., 2009). In particular, the timescales of partial melting in high-grade metamorphic rocks, when they begin to melt in a collision cycle and how long they remain partially molten, can be central to understanding the architecture and deformation of collisional orogenic belts. The Himalayan orogen, the result of the ongoing Cenozoic collision of the Indian and Asian plates, exposes a spectacular assemblage of migmatites and leucogranites (e.g., Kohn, 2014; Yin & Harrison, 2000). These rocks, which represent the buried and subsequently exhumed Indian continental crust, are an ideal vehicle to study active orogenic processes and test geodynamic models of how the crust responds to continental collision (e.g., Guillot et al., 2008; Kohn, 2014; Searle et al., 2011). Although the timing and conditions of crustal melting in the Himalayan orogen, especially its core, have been intensively studied, interpretations of how that melt has affected the overall deformation behavior of the orogen differs substantially. For example, some have advocated for critical taper-like behavior (cooler P-T conditions, in-sequence thrusting, decreasing P-T conditions, and ages structurally downward) with little direct influence of melt on structure, while others have advocated for channel-flow behavior (warmer P-T conditions, nearly synchronous exhumation of a large thickness of crust), driven by coupling of the flow of weak migmatites to an erosional front (see detailed reviews of Himalayan high-grade metamorphism and tectonics in Kohn, 2014 and Carosi et al., 2018). In the Sikkim-Yadong region, eastern Himalaya, well-exposed migmatites and leucogranites indicate intense anatexis of the orogenic core (e.g., Chakraborty et al., 2016, 2017; Harris et al., 2004; Kellett et al., 2013; Rubatto et al., 2013;

Searle & Szulc, 2005; Sorcar et al., 2014; Z. Zhang et al., 2017; Z. M. Zhang et al., 2017). They therefore offer an excellent opportunity to study the timing and duration of metamorphism, partial melting, and melt crystallization of the Himalayan orogen in the context of its structural evolution.

In this study, to better understand the timescales over which partial melt was produced and crystallized during the Himalayan orogeny, we present a systematic data set of cathodoluminescence (CL) images, U-Pb ages, and trace element compositions of zircon from migmatitic pelitic granulite and associated leucosomes in the Yadong region, eastern Himalaya, immediately east of Sikkim. Our new work builds on a prior study of the granulite (Z. Zhang et al., 2017) that developed a robust P-T path through thermodynamic modeling, and identified the general timescale of metamorphism. Here, we add a much more comprehensive data set of zircon ages and compositions for associated leptosomatic rocks (e.g., discovering an age gap between 24 and 22 Ma that was not recognizable with fewer prior data) and explore tectonic implications more thoroughly. These new data show that the pelitic granulite underwent prolonged high-temperature metamorphism and anatexis. Three stages of melt evolution include prograde melting with increasing temperature between ~32 and 24 Ma, decompression melting between ~22 and 19 Ma, and melt crystallization between ~19 and 13 Ma. We suggest that intensive melting and initiation of melt segregation may have triggered the formation of Himalayan leucogranites and exhumation of mid-lower crustal rocks by altering the strength profile of the crust.

2. Geological Setting

The 2,500-km-long Himalayan orogen is separated tectono-stratigraphically by the north-dipping South Tibetan Detachment System (STDS), Main Central Thrust (MCT), and Main Boundary Thrust (MBT). These structures divide the orogen from north (structurally highest) to south (structurally lowest) into the Tethys Himalayan Sequence (THS, above the STDS), Greater Himalayan Sequence (GHS, between the STDS and MCT), Lesser Himalayan Sequence (LHS, between the MCT and MBT) and Sub-Himalayan Sequence (below the MBT; e.g., Yin & Harrison, 2000; Yin, 2006; Figure 1a). Oligocene-Miocene leucogranite dikes and plutons mainly intruded the upper part of the GHS, or into the THS (e.g., Guo & Wilson, 2012; Le Fort et al., 1987; Searle et al., 1997; Searle & Godin, 2003; Weinberg, 2016; Wu et al., 2015). The STDS is characterized by a several hundred meters to kilometer thick ductile to brittle shear zone with a top-to-the-north shear sense, and is commonly regarded as a detachment fault system. Ductile shear along the STDS occurred between 25 and 16 Ma and was accompanied by emplacement of leucogranite plutons (e.g., Chambers et al., 2011; Cottle et al., 2007; Kellett et al., 2018; Leloup et al., 2010; Searle & Godin, 2003; Yin, 2006). The MCT is characterized by a kilometer-scale thrust-sense ductile shear zone (Yin, 2006; Yin & Harrison, 2000). In addition to these structures, major thrust-sense shear zones also occur within the GHS and many have been correlated along-strike with the High Himalayan Discontinuity (HHD) in Nepal (see reviews of Carosi et al., 2018; Cottle et al., 2015; Montomoli et al., 2015). These intra-GHS shear zones are thought to have been active before the MCT, at 25 to 20 Ma versus ≤20 Ma (e.g., Carosi et al., 2018; Kohn, 2008).

In terms of metamorphism, the LHS preserves a nearly orogen-scale classic inverted Barrovian sequence from chlorite to kyanite zones, where higher metamorphic grades lie successively at higher structural levels (generally south to north; e.g., Colchen et al., 1986; Dasgupta et al., 2004, 2009; Gaidies et al., 2015; Harrison et al., 1998; Kohn, 2008, 2014; Mohan et al., 1989; Mottram et al., 2014). The lithology of the GHS in different areas varies significantly, but in general, the lower to middle structural level of the GHS consists of upper amphibolite to granulite-facies metasediments and granitic orthogneisses, and contains abundant concordant and discordant felsic horizons and lenses (e.g., Le Fort, 1975). Both metasediments and orthogneisses underwent dehydration melting of muscovite and biotite (see review of Kohn, 2014). The upper structural level of the GHS consists mainly of metapelites schists and gneisses, with minor quartzites, marbles, calc-silicate rocks, and (rare) metabasites, hosting networks and lens-shaped bodies of leucogranites (e.g., Colchen et al., 1986; Le Fort, 1975; Murphy & Harrison, 1999; Searle et al., 2003).

The Sikkim-Yadong region of the eastern Himalaya exposes the inverted metamorphic sequence, major structures (MCT, STDS, and HHD), and GHS high-grade metamorphic rocks and leucogranites that are so characteristic of Himalayan structure and metamorphism (Figure 1b; Catlos et al., 2004; Chakraborty

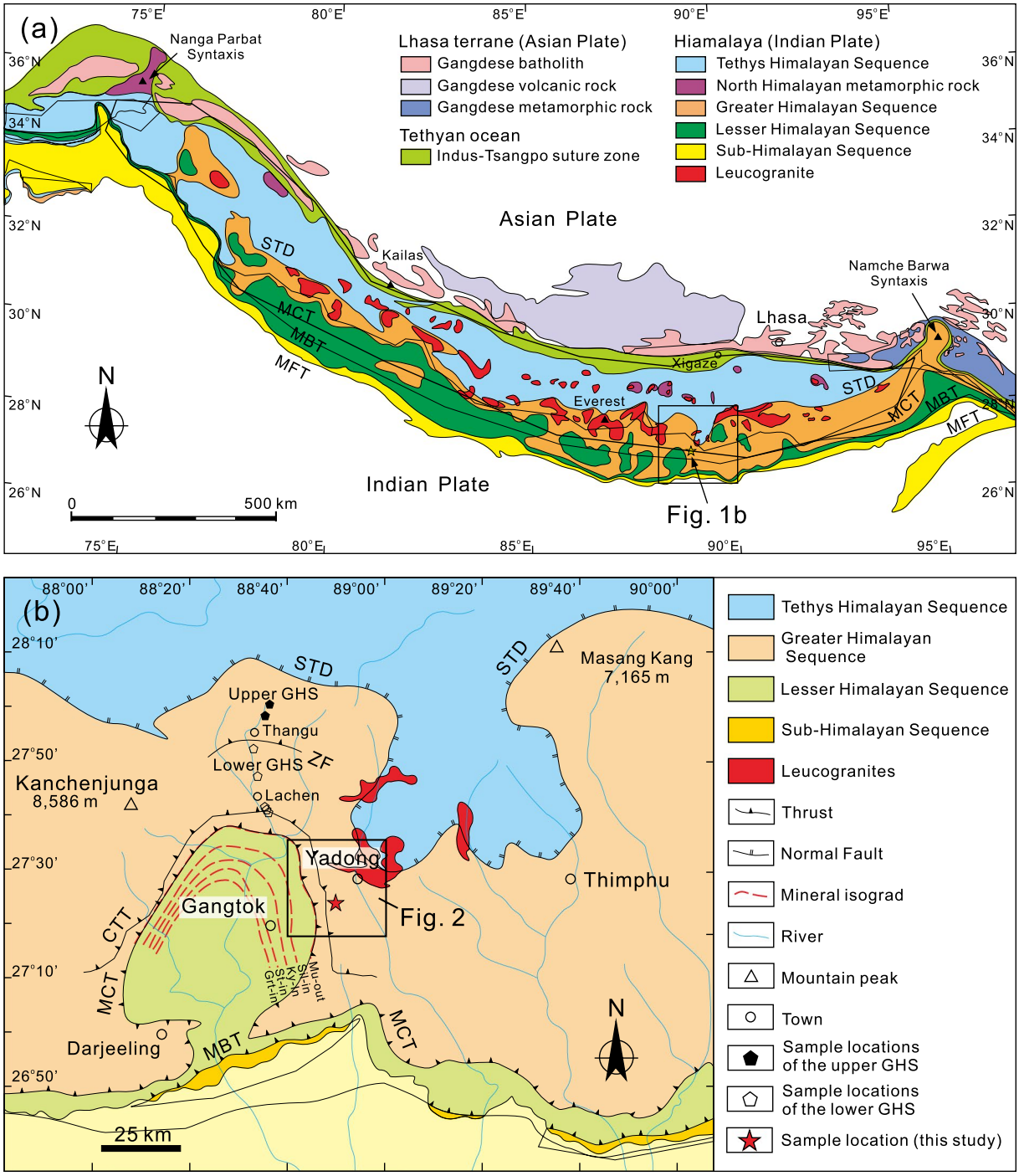

Figure 1. (a) Geological map of the Himalayan orogen (modified after Yin & Harrison, 2000) showing regional distribution of the main rock units and structures, and location of our study area. (b) Simplified geological map of Sikkim-Yadong area, showing the local distribution of rock units and structures, and the sample location. Mineral isograds and samples of lower and upper GHS (Greater Himalayan Sequence) are after Rubatto et al. (2013). Zema Fault (ZF) and Chungthang-Thambi Thrust (CTT) represent tectonometamorphic discontinuities within the GHS proposed by Rubatto et al. (2013) and Chakraborty et al. (2019), respectively. MBT, Main Boundary Thrust; MCT, Main Central Thrust; STD, South Tibetan Detachment.

et al., 2016, 2017, 2019; Dasgupta et al., 2004, 2009; Gaidies et al., 2015; Rubatto et al., 2013; Sorcar et al., 2014; Z. Zhang et al., 2017; Z. M. Zhang et al., 2017). In this area, the GHS consists mainly of schists and paragneisses, although orthogneisses and leucogranites dominate the upper part (Figure 2, Gou et al., 2015). These metamorphic rocks experienced granulite-facies metamorphism (e.g., Rubatto et al., 2013; Sorcar

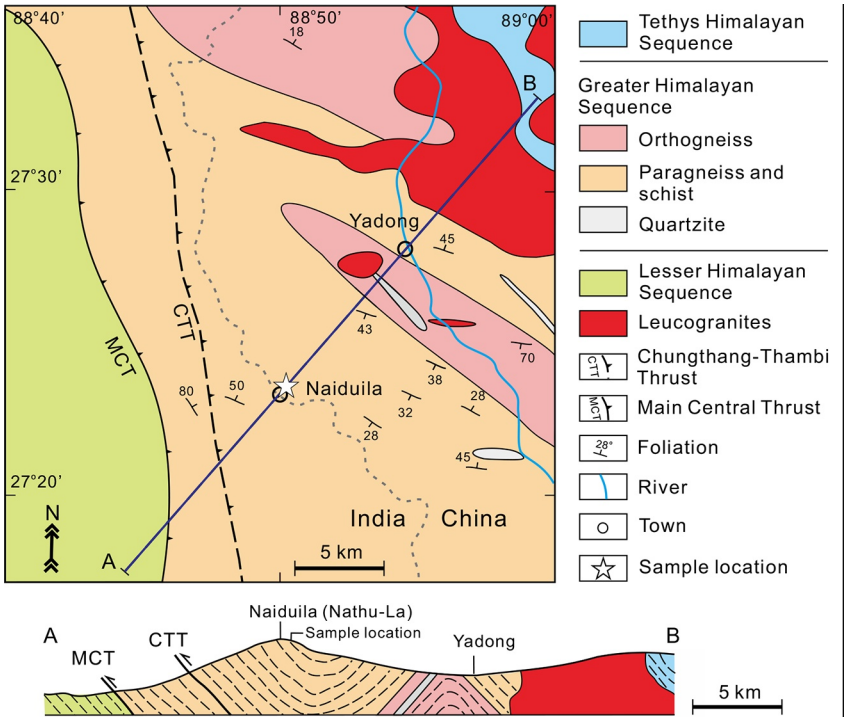

Figure 2. Simplified geological map (upper part) and cross-section (lower part) of the Yadong area, showing sampling site near to the China-India (Sikkim) boundary.

et al., 2014; Z. Zhang et al., 2017; Z. M. Zhang et al., 2017) and consist of melanosome (dominated by biotite, garnet, plagioclase, sillimanite, and kyanite) and millimeters- to centimeters-thick leucosome (dominated by quartz, plagioclase, and K-feldspar). Recently, Chakraborty et al. (2019) identified a 1- to 5.6-km-wide shear zone, the Chungthang-Thambi thrust (CTT, Figures 1b and 2), within the lower level of the GHS. Chakraborty et al. (2019) correlate this structure with the intra-GHS (HHD), and argue for ductile shearing between ca. 27 Ma and ca. 22.5 Ma, overprinted by later brittle deformation.

3. Petrology

The present investigation focuses on a nearly leucosome-devoid migmatitic pelitic granulite (sample 16-8) and six associated leucosomes (samples 15-4, 50-3, 50-5, 50-6, 50-7, and 50-12) to the GHS. These rocks represent the hanging wall of the CTT (HHD) at the upper structural level exposed to the GHS (Figures 1b and 2). All samples were collected from a locality 15 km to the southwest of the town of Yadong, on the Chinese side of the China-India border with a GPS position of N27°23′54″ and E88°50′28″ (Figures 1b and 2). At the outcrop scale, the granulite consists of planar-foliated, dark, biotite + plagioclase + sillimanite + garnet melanosome, alternating with leucosome (Figure 3a). Leucosomes occur as cm- to a few dm-scale in situ (negligibly mobilized) and in-source (locally coalesced) lenses or veins that consist mainly of plagioclase, K-feldspar, and quartz (Figures 3a and 3b). Some leucosomes contain small slices of melanosome. Textures and mineralogy indicate that the leucosomes were derived from partial melting of the pelitic granulite and experienced variable but small degrees of melt segregation (e.g., see Brown et al., 1995). Z. Zhang et al., 2017 reported the petrology, general geochronology, and P-T path of the granulite sample (16-8), and the CL images and geochronologic data of zircon for that sample are after Z. Zhang et al. (2017).

The pelitic granulite is schistose and consists of plagioclase, biotite, garnet, quartz, and sillimanite, with minor kyanite, K-feldspar, cordierite, rutile, and ilmenite (Figures 4a and 4b). Garnet occurs as porphyroblasts with inclusions of kyanite, plagioclase, biotite, muscovite, and quartz. Kyanite and muscovite occur

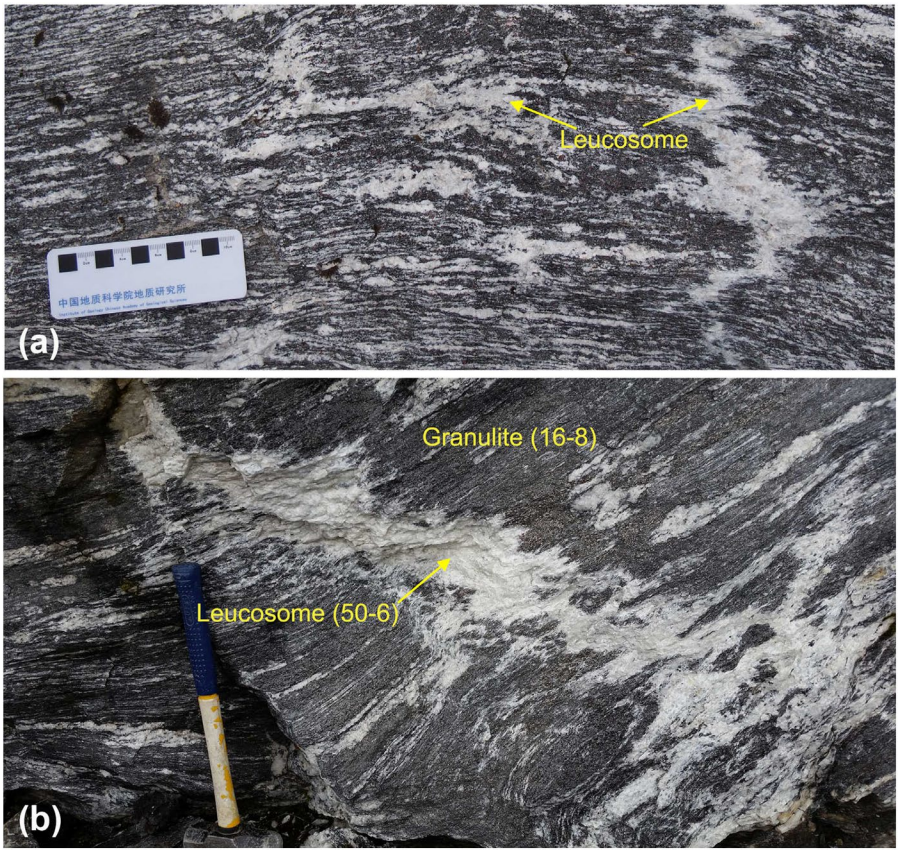

Figure 3. Field photos of the migmatitic pelitic granulite and associated leucosomes. (a) The pelitic granulite consists of biotite, plagioclase, and quartz with minor garnet and sillimanite, whereas the leucosome occurs as concordant and discordant bands and veins within the granulite and consists of plagioclase, K-feldspar, and quartz with minor garnet and biotite. These mineralogies and textures are consistent with segregation of anatectic melts to form foliation-parallel and locally connecting leucosomes. (b) The pelitic granulite consists mainly of biotite, plagioclase, and quartz, and contains concordant and discordant leucosome veins that consist mainly of plagioclase, K-feldspar, and quartz with minor biotite. Locations of samples of leucosome (50-6) and pelitic granulite (16-8) are radiolabeled. The hammer for scale is 27 cm in length.

only as inclusions within the garnet. Biotite occurs as inclusions in the garnet and in the matrix. Sillimanite occurs only in the matrix. Garnet is partly replaced by biotite + plagioclase + sillimanite ± cordierite along its rims, while biotite is replaced by sillimanite along its edges (Figures 4a and 4b). These micro-textures indicate that an earlier, higher-pressure mineral assemblage of garnet + kyanite + biotite + plagioclase + quartz ± muscovite ± K-feldspar was replaced by a later, lower-pressure assemblage of garnet + sillimanite + biotite + plagioclase + cordierite + quartz (Z. Zhang et al., 2017). Rubatto et al. (2013) and Sorcar et al. (2014) report similar assemblages and textures nearby in Sikkim, but infer much lower peak pressures. The studied leucosome assemblage of plagioclase, K-feldspar, and quartz, with minor biotite, cordierite, sillimanite, and garnet (Figures 4c–4f) is consistent with derivation by partial melting of the host granulite (Z. Zhang et al., 2017).

4. Prior P-T Path Interpretation

Phase equilibrium models of the pelitic granulite were calculated by Z. Zhang et al. (2017) using a melt-reintegrated bulk composition in the system MnO-Na_2O-CaO-K_2O-FeO-MgO-Al_2O_3-SiO_2-H_2O-TiO_2-O_2 (MnNCKFMASHTO). In the context of these models and petrographic observations, especially the occurrence of rutile and kyanite inclusions in garnet, a peak metamorphic assemblage can be inferred: Bt + Pl + Kf + Grt + Ky + Qz + Rt + Ilm (+melt; Z. Zhang et al., 2017; Figure 4). This assemblage is stable at high-pressure

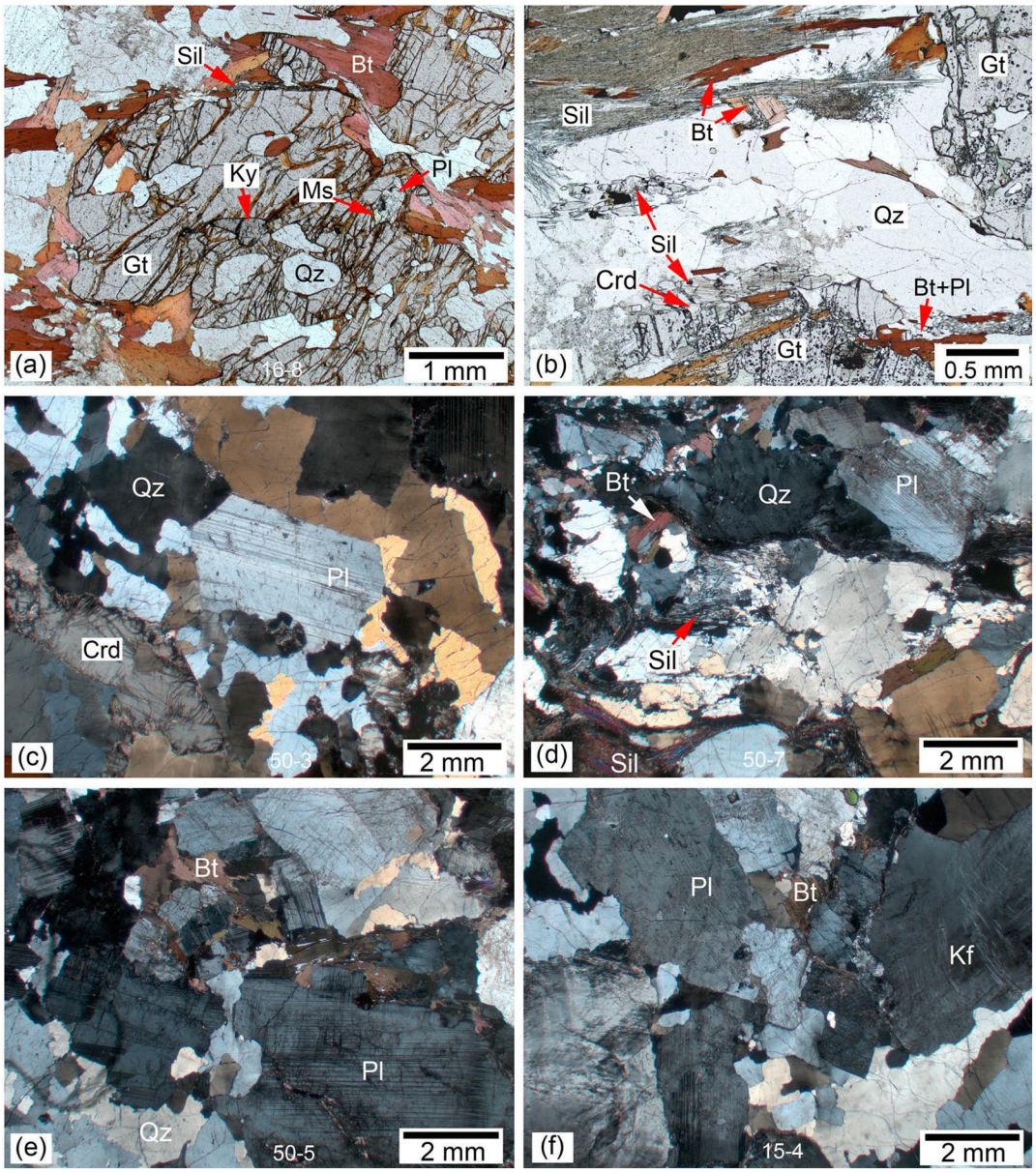

Figure 4. Photomicrographs of the migmatitic pelitic granulite and leucosomes using plane-polarized light (a–b) and cross-polarized light (c–f). (a) Pelitic granulite (sample 16-8) contains garnet, plagioclase, biotite, and quartz with minor K-feldspar, kyanite, and sillimanite. Kyanite and muscovite occur only as inclusions within garnet porphyroblasts, whereas sillimanite occurs along the margins of garnet and biotite. (b) In pelitic granulite (sample 16-8), porphyroblastic garnets are partly replaced by biotite + plagioclase + sillimanite + cordierite along their edges, and biotite grains are replaced by sillimanite along their margins. (c)–(f) Leucosome samples (50-3, 50-7, 50-5, and 15-4, respectively) consist mainly of plagioclase, quartz, and K-feldspar. Some samples contain minor biotite, sillimanite, and cordierite. Mineral abbreviations: Bt, biotite; Crd, cordierite; Gt-garnet, Kf, K-feldspar; Ky-kyanite; Ms, muscovite; Pl, plagioclase; Qz, quartz; Sil-sillimanite.

granulite-facies condition of 12.0–15.5 kbar and 820–870°C. In contrast, the observed matrix (retrograde) assemblage–Bt + Pl + Grt + Sil + Crd + Qz + Ilm (Figure 4b), is stable at LP granulite-facies condition of <6.6 kbar and 700–850°C (Figure 5). Thus, the pelitic granulite records a clockwise P-T path, characterized by heating and burial to high-pressure granulite-facies conditions, subsequent approximately isothermal decompression, and approximately isobaric cooling (Figure 4; Z. Zhang et al., 2017). As we discuss below, our new zircon petrochronological results reinforce this P-T path.

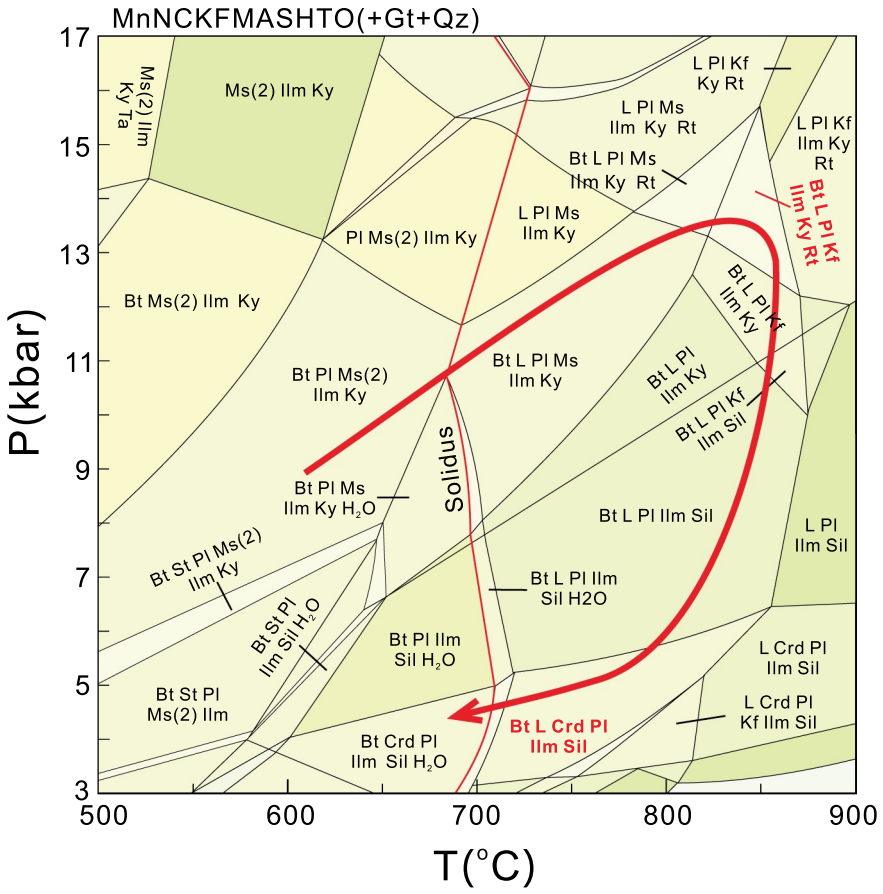

Figure 5. P-T pseudosection of the pelitic granulite modeled using the melt-reintegrated bulk composition (recalculated after Z. Zhang et al., 2017). The peak and retrograde mineral assemblages are shown by the bold red fonts. The bold red line with arrow is the metamorphic P-T path. Darker shaded fields have fewer stable minerals. Mineral abbreviations: Bt, biotite; Crd, cordierite; Gt, garnet; Ilm, ilmenite; Kf, K-feldspar; Ky, kyanite; L, liquid; Ms, muscovite; Pl, plagioclase; Qz, quartz; Rt, rutile; Sil, sillimanite; St, staurolite; Ta, talc.

5. Analytical Methods

In-situ zircon U-Pb dating and trace element analysis were simultaneously conducted by LA-ICP-MS at the Wuhan Sample Solution Analytical Technology Co., Ltd. Intracrystalline domains with uniform CL intensity or composition (Figure 6) were targeted for analysis. Detailed operating conditions for the laser ablation system and the ICP-MS instrument and data reduction are the same as described by Zong et al. (2017). Laser sampling was performed using a GeolasPro laser ablation system that consists of a COMPexPro 102 ArF excimer laser (wavelength of 193 nm and maximum energy of 200 mJ) and a MicroLas optical system. An Agilent 7700e ICP-MS instrument was used to acquire ion-signal intensities. Helium was applied as a carrier gas. Argon was used as the make-up gas and mixed with the carrier gas via a T-connector before entering the ICP. A "wire" signal smoothing device is included in this laser ablation system (Hu et al., 2015). The spot size and frequency of the laser were set to 32 or 24 μm and 5 Hz, respectively.

Zircon 91500 was used as an external standard for U-Pb dating, with zircons GJ-1 and Plešovice as check standards. Glass NIST610 and SiO_2 (32.7 wt%) were used for trace element external calibration and internal standardization, respectively. The obtained weighted mean $^{206}Pb/^{238}U$ ages for zircon standards GJ-1 and Plešovice were 601.3 ± 3.4 Ma (95% confidence limits, $n = 16$, MSWD = 0.70) and 336.7 ± 1.7 Ma (95% confidence limits, $n = 16$, MSWD = 0.71), respectively (Table S1). These comparisons are consistent with recommended values (602.1 ± 4.9 Ma for GJ-1, Liu et al., 2010; 337.1 ± 0.37 Ma for Plešovice, Sláma et al., 2008), and demonstrate that our calibration is accurate to ±0.5%. This propagated calibration error is strongly subsidiary to age precision (on average ~5% or ~1 Ma, 2σ; Table S1) and is not considered in our interpretations.

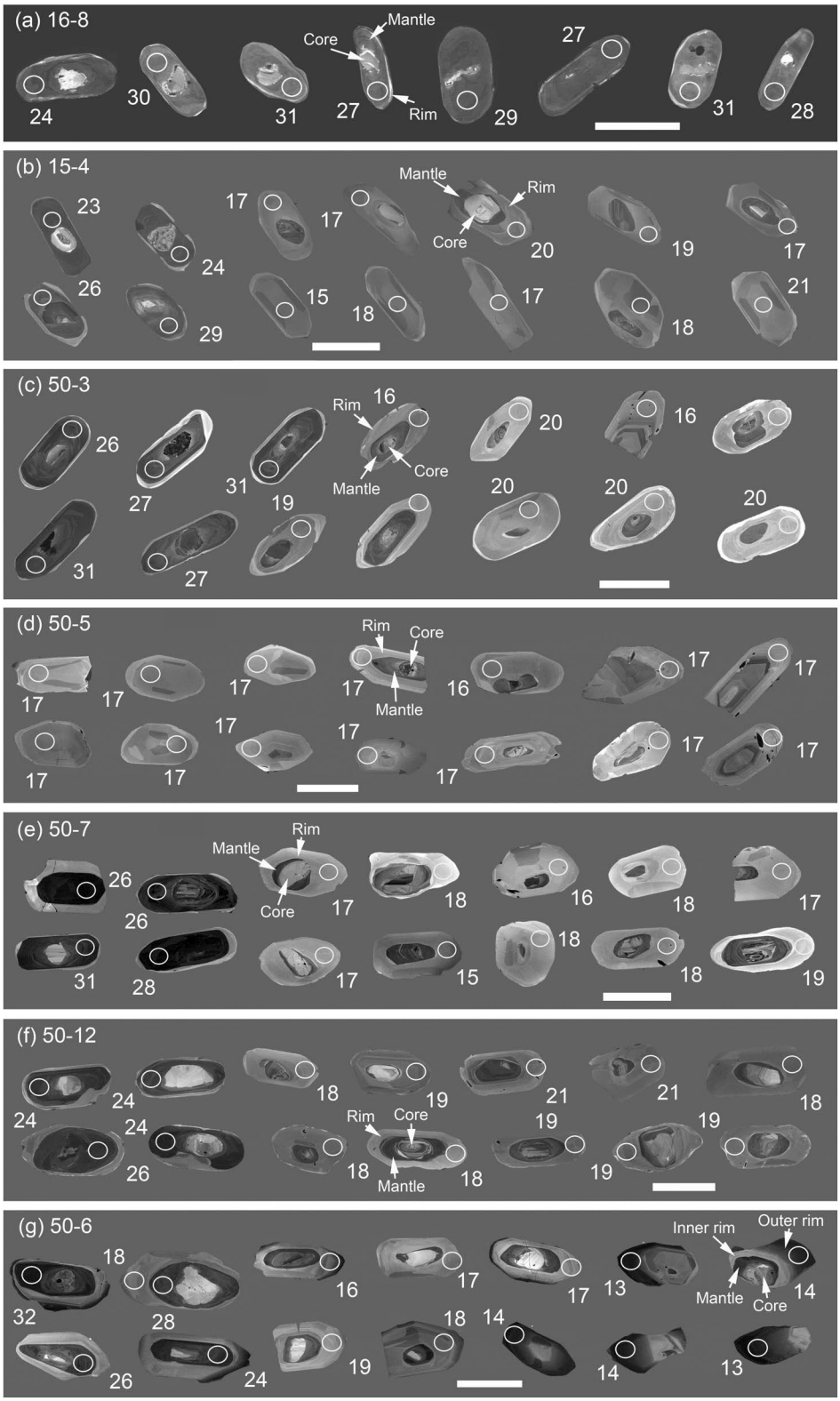

Figure 6. Cathodoluminescence (CL) images of zircon, showing the analyzed spot locations and relevant ages (in Ma). (a) Pelitic granulite and (b)–(g) leucosomes. The core, mantle, and rim structure of zircon is marked in a representative grain for each sample. All scale bars are 100 μm. CL, Cathodoluminescence.

Each analysis incorporated a background acquisition of approximately 20–30 s followed by 50 s of data acquisition from the sample. These conditions yielded pit depths of ~10 μm. An Excel-based software ICPMS-DataCal was used to perform off-line selection and integration of background and analyzed signals, time-drift correction, and quantitative calibration for trace element analysis and U-Pb dating (Liu et al., 2010). Alternate data processing software (Iolite) does not yield significantly different results. All traces of the data presented in Table S1 were verified for flat signals to ensure that ablation did not inadvertently intersect an inclusion or fracture, or create mixed analyses by penetrating compositionally and chronologically different domains below the imaged surface. Any questionable traces (humps, troughs, oscillations, abrupt shifts, etc.) were eliminated. Concordia diagrams and weighted mean calculations were made using Isoplot/Ex_ver 4 (Ludwig, 2003).

6. Results

6.1. Internal Structure of Zircon

Zircon in both pelitic granulite and leucosome occurs as matrix grains or as inclusions within garnet, plagioclase, and biotite. Zircon grains from both the granulite and leucosome are colorless, euhedral to subhedral, and prismatic, and exhibit a typical core-mantle-rim structure in CL images (Figure 6), although inherited core or mantle domains are missing in some grains, and rims can be very thin.

Zircon in the granulite has small inherited detrital cores, wide mantles, and very narrow rims (Figure 6a; Z. Zhang et al., 2017). The core domains show light luminescence. The mantle domains are generally CL dark and either show weak patchy zoning or are unzoned. The narrow rims show light luminescence. These rims were too thin to analyze, which is what prompted us to sample leucosomes in search of thicker rims that could be analyzed to learn more about the later-stage evolution of these rocks.

Zircon separated from leucosomes has small inherited cores with variable shape, luminescence and zoning, wide mantles, and narrow to wide rims. Similar to zircons that were directly sampled from the host rock granulite, the mantle domains in leucosome zircon show very dark luminescence and weak patchy and oscillatory zoning or are unzoned. Thick rims show light luminescence and weak patchy or oscillatory zoning (Figures 6b–6f). The zircon from the leucosome sample 50-6 shows the same core-mantle-rim structure as zircons from other rocks, but the rim can be divided into an inner rim with light luminescence and weak patchy or oscillatory zoning, like the rims of the zircon from other leucosome samples, and an outer rim with very dark luminescence and lack of zoning (Figure 6g).

6.2. U-Pb Ages of Zircon

Zircon analyses from the granulite ($n = 14$) and leucosomes ($n = 223$) yielded variable $^{206}Pb/^{238}U$ ages ranging from 32 to 13 Ma that are all concordant within uncertainty (Figures 7, 8, and 9a; Table S1). The zircon mantle domains of the granulite and leucosomes are relatively old, ranging from 29 to 20 Ma and 32 to 24 Ma, respectively (Figures 7, 8, and 9a; Table S1). The zircon rim and inner rim domains of the leucosomes range in age from 22 to 14 Ma (Figures 7, 8, and 9a; Table S1), whereas the outer rim domains of zircons from leucosome sample 50-6 have the youngest ages ranging from 14 to 13 Ma (Figure 8e; Table S1). Two age population clusters occur at ~26 Ma and ~17 Ma (Figure 9b), respectively. A distinct age gap is observed between 24 and 22 Ma that corresponds with the boundary between the mantle and rim domains of zircons from the leucosomes (Figures 9a and 9b).

6.3. Trace Elements of Zircon

Trace element concentrations and ratios in zircon analyses are presented in Table S1 and vary substantially (over an order of magnitude for many elements), but nonetheless show patterns in scatter and slope (Figures 7–10), organized according to age and CL domain.

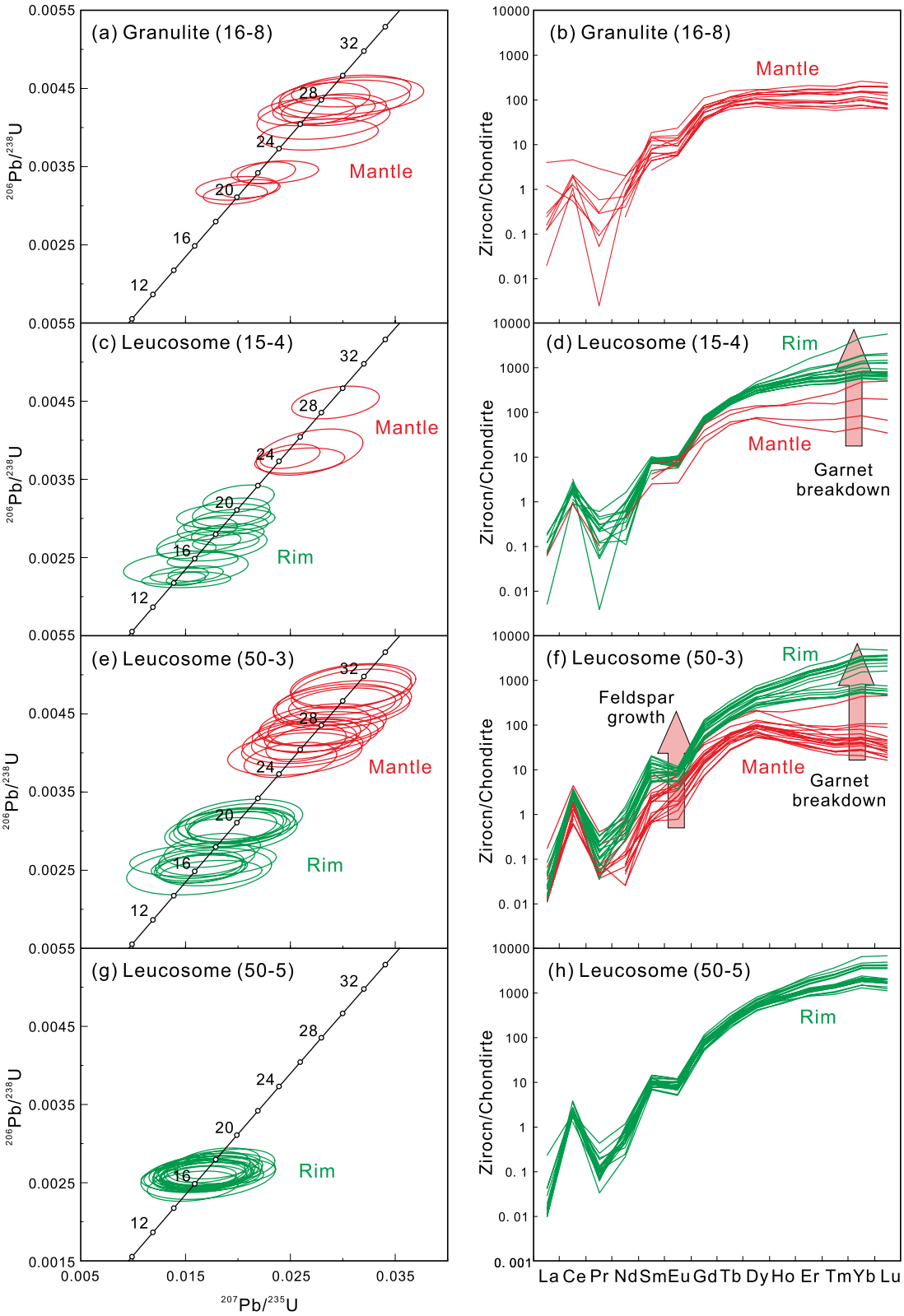
(a) Granulite (16-8)
(b) Granulite (16-8)
(c) Leucosome (15-4)
(d) Leucosome (15-4)
(e) Leucosome (50-3)
(f) Leucosome (50-3)
(g) Leucosome (50-5)
(h) Leucosome (50-5)
Mantle
Rim
Feldspar growth
Garnet breakdown
$^{206}Pb/^{238}U$
$^{207}Pb/^{235}U$
Zirocn/Chondirte
La Ce Pr Nd Sm Eu Gd Tb Dy Ho Er Tm Yb Lu

6.3.1. 32–24 Ma (Mantle Domain)

Th and Th/U increase strongly (Figures 10a and 10c); U, Y, and heavy rare earth elements (HREEs) increase slightly (Figures 10b–10e); Eu/Eu*, Hf, Nb, Ta, and Nb/Ta show large scatter (Figures 10f–10j); HREE patterns are flat (Figures 7, 8, and 9c).

6.3.2. 24–22 Ma (Age Gap Between Mantle and Rim)

Comparing trends before 24 Ma and after 22 Ma, the following changes are observed across the age gap: a change in slope for Th and U (Figures 10a and 10b); a compositional offset for Y and HREE (Figures 10d and 10e); and decreased scatter for Eu/Eu* (Figure 10f), Hf, Nb, Ta, and Nb/Ta (Figures 10g–10j). The steepness of HREE also increases (Figures 7, 8, and 9c).

6.3.3. 22–19 Ma (Rim and Inner Rim)

Th/U, Y, and HREE increase while Eu/Eu* decreases.

6.3.4. 19–14 Ma (Rim and Inner Rim)

The slope for Y and HREE steepens (Figures 10d and 10e), while Th/U switches trend (decreases, some spots show sharp decreases; Figure 10c) and Eu/Eu* continues to decrease (Figure 10f).

6.3.5. 14–13 Ma (Rim and Outer Rim)

The following changes are observed: A large change in slope for U (Figure 10b), possibly Y + HREE (Figures 10d and 10e), Hf, Ta, and Nb/Ta (Figures 10g–10j); an offset for Eu/Eu* (Figure 10f); and increased steepness of HREE (Figure 10e).

7. Discussion

7.1. Zircon Petrochronologic Interpretation

A rigorous interpretation of zircon ages requires relating the different domains to specific metamorphic stages and, ideally, to specific reactions. Particularly important is to determine whether zircon formed during prograde metamorphism, melting at or near peak temperature, or during retrograde overprint at super- or sub-solidus conditions (Kohn & Kelly, 2018; Rubatto, 2017; Rubatto et al., 2013). Accessory mineral modeling demonstrates that, from a mass balance perspective, the mode of zircon cannot increase during prograde metamorphism and melting (Kelsey et al., 2008; Kelsey & Powell, 2011; Kohn et al., 2015). Increases in abundances of garnet, rutile, and melt must result in a net decrease in the volume of zircon. Yet, zircon grains commonly show age- and CL-distinct domains with chemistry or mineral inclusions that are consistent with the formation during prograde metamorphism or melting (Kohn & Kelly, 2018; Rubatto, 2017). The volume of zircon that is remobilized and reprecipitated during prograde metamorphism also far exceeds the amount needed to explain Zr contents in other minerals plus melt. Thus, some zircon crystals form and preserve domains during prograde metamorphism and melting, even as the overall abundance of zircon decreases. These domains are interpreted to form by dissolution-reprecipitation and/or Ostwald ripening (see summaries of Rubatto, 2017; Kohn and Kelly, 2018; also Nemchin et al., 2001). Subsolidus zircon domains that precipitate from aqueous solutions typically contain microporosity and microinclusions of U-Th-HREE minerals (thorite, xenotime, etc.), whereas zircon domains that precipitate in the presence of a melt generally lack these features (Kohn & Kelly, 2018; Rubatto, 2017). Zircon domains in

Figure 7. U-Pb concordia diagrams (left columns) and chondrite-normalized REE patterns (right columns) of zircon. (a) and (b) Zircons from pelitic granulite represent a single textural domain (mantle). These show sparse ages with an age gap between about 22 and 26 Ma, and moderate HREE contents with flat patterns. (c)–(h) Zircons from the leucosomes represent multiple textural domains. Mantle versus rim domains show systematic age differences with an age gap between about 22 and 24 Ma. Pink arrows indicate increasing HREE contents and deepening negative Eu anomalies from mantle to rim, implying garnet breakdown and plagioclase growth, respectively, during retrograde metamorphism and melt crystallization.

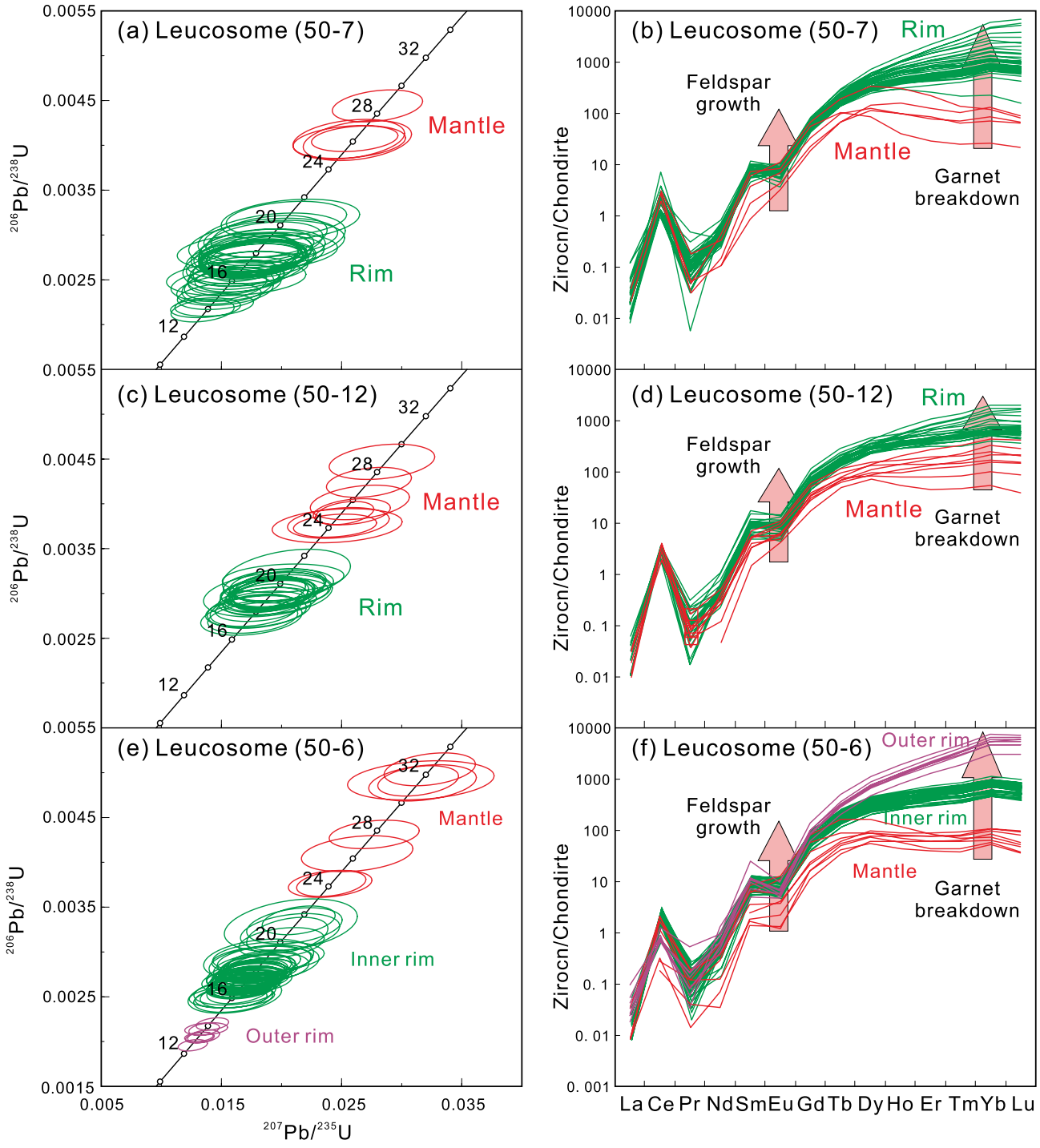

Figure 8. U-Pb concordia diagrams (left columns) and chondrite-normalized REE patterns (right columns) of zircon from the leucosomes. Zircons from these leucosomes represent multiple textural domains. Mantle versus rim domains show systematic age differences with an age gap between about 22 and 24 Ma. Chemically zoned rims show an age range from about 15 to 13 Ma. Pink arrows indicate increasing HREE contents and deepening negative Eu anomalies from mantle to rim, implying garnet breakdown and plagioclase growth, respectively, during retrograde metamorphism and melt crystallization.

the studied samples show no microporosity or unusual microinclusions (Figure 6). These textures suggest formation in the presence of a melt, but we further use chemistry to interpret the conditions of formation of these domains.

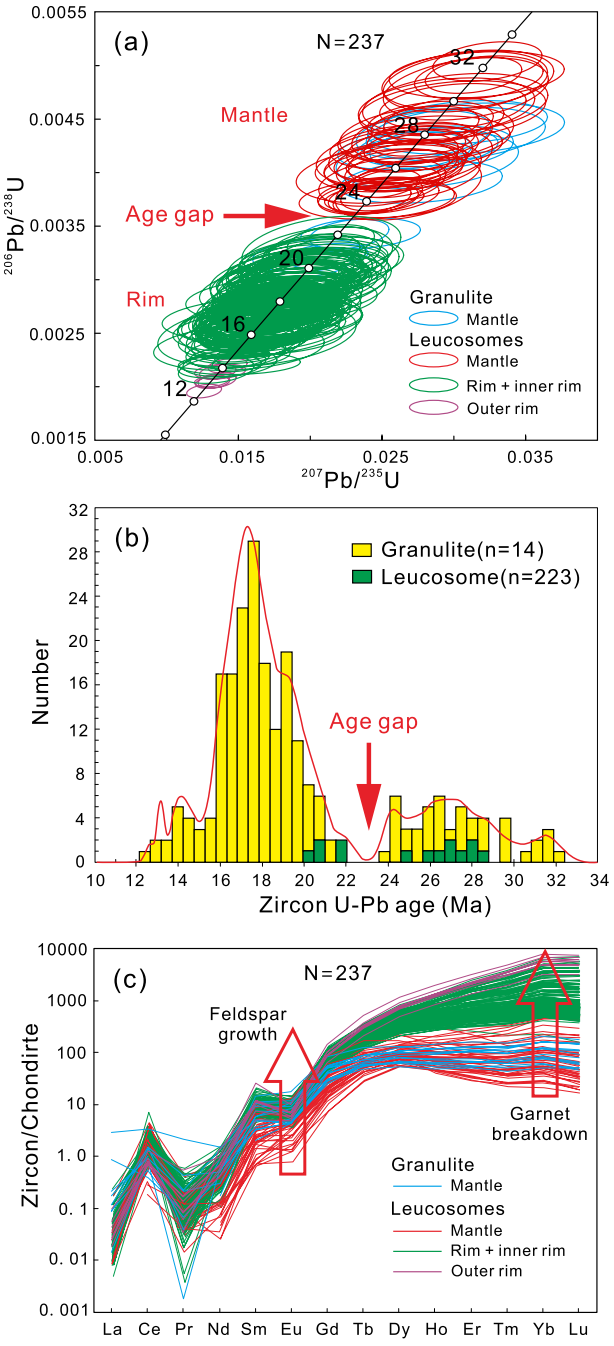

Figure 9. Summary diagrams for all zircon age and REE data. (a) U-Pb Concordia diagram shows a nearly continuous distribution of ages from 32 to 13 Ma, but with a distinct age gap between 24 and 22 Ma, corresponding generally to mantle versus rim domains. (b) U-Pb age relative probability diagram shows the 24–22 Ma age gap and a pronounced peak in age at ca.17 Ma. (c) Chondrite-normalized REE pattern. Red arrows indicate increasing HREE contents and deepening negative Eu anomalies, implying garnet breakdown and plagioclase growth, respectively, during retrograde metamorphism and melt crystallization.

Petrographically, we observe only one episode of garnet growth and consumption in the studied granulite, and geochemically we observe no multiple clustering of ages or oscillations in Th/U, Y, HREE, and Eu/Eu* (Figures 9a and 10c–10f). Consequently, we interpret these zircons to have formed during only one continuous process of metamorphism, anatexis, and melt crystallization, rather than multiple cycles of temperature change or melt production, loss, crystallization, and so on. The similarity in CL textures, ages, and trace element compositions among zircons separated from granulite versus leucosome (Figures 6–10; Table S1) is consistent with the derivation of both rock types and their zircons from the same precursor. Consequently, we interpret all zircon ages and compositions together and do not parse data according to hand specimen or rock type. In general, we interpret the chemical trends in mantle and rim zones of zircons in the context of major and trace phase abundances and overall P-T evolution, according to the following principles:

1. Melting dissolves monazite preferentially compared to zircon (Kelsey et al., 2008; Yakymchuk & Brown, 2014), and because monazite preferentially incorporates Th relative to U, increased melting should produce higher Th/U in zircon (Yakymchuk & Brown, 2019; Yakymchuk et al., 2018). Conversely, melt crystallization should result in lower Th/U in zircon
2. Plagioclase strongly partitions Eu^{2+} compared to other phases, including melt (the partition coefficient, D, is approximately 2), whereas K-feldspar moderately partitions Eu^{2+} ($D \sim 0.75$), and other phases take very little (Holder et al., 2020). In our models, K-feldspar is never modally abundant, and any growth is more than offset by dissolution of plagioclase (Figures 11a and 11b). Thus, decreasing Eu/Eu* indicates increasing abundance of plagioclase, but not K-feldspar. Changes to redox state (Eu^{2+}/Eu^{3+}) also depend on pressure (Holder et al., 2020), but predicted changes to Eu/Eu* for very large changes to pressure are only ~20%–30% (Holder et al., 2020), whereas we observe changes of a factor of ~2–3 (Figure 10f)
3. Garnet, allanite, and xenotime take up substantial Y and HREE (Engi, 2017; Hermann, 2002; Spear & Pyle, 2002), but there is no petrographic evidence for prograde allanite or xenotime in the studied rocks. So, lower Y and HREE of zircon and a flatter slope to HREE trends mainly reflect garnet growth. However, increasing temperature might cause diffusional loss of Y and HREE from garnet cores (e.g., 700°C–900°C; Carlson, 2012; Kohn, 2009), increasing the HREE and Y content of the reactive rock. In general, we expect that garnet growth should lead to steadily decreasing Y and HREE availability, while dissolution of garnet (and possibly stasis at very high temperature of ≥~700°C; Ding et al., 2021) should lead to increasing Y and HREE availability. Dissolution of monazite will also increase available Y and HREE, but in general garnet growth and consumption dominate the mass balance of these elements (Spear & Pyle, 2010)
4. High field strength elements (Hf, Nb, and Ta) depend on abundances of biotite, rutile, and ilmenite (e.g., Luvizotto & Zack, 2009), but because partition coefficients are not well known, we are as yet unable to independently interpret Hf, Nb, Ta, and Nb/Ta trends. Trends generally parallel other trace elements or show changes in slope at similar times (Figures 10g–10j), indicating that Hf, Nb, and Ta likely respond to melt production and crystallization

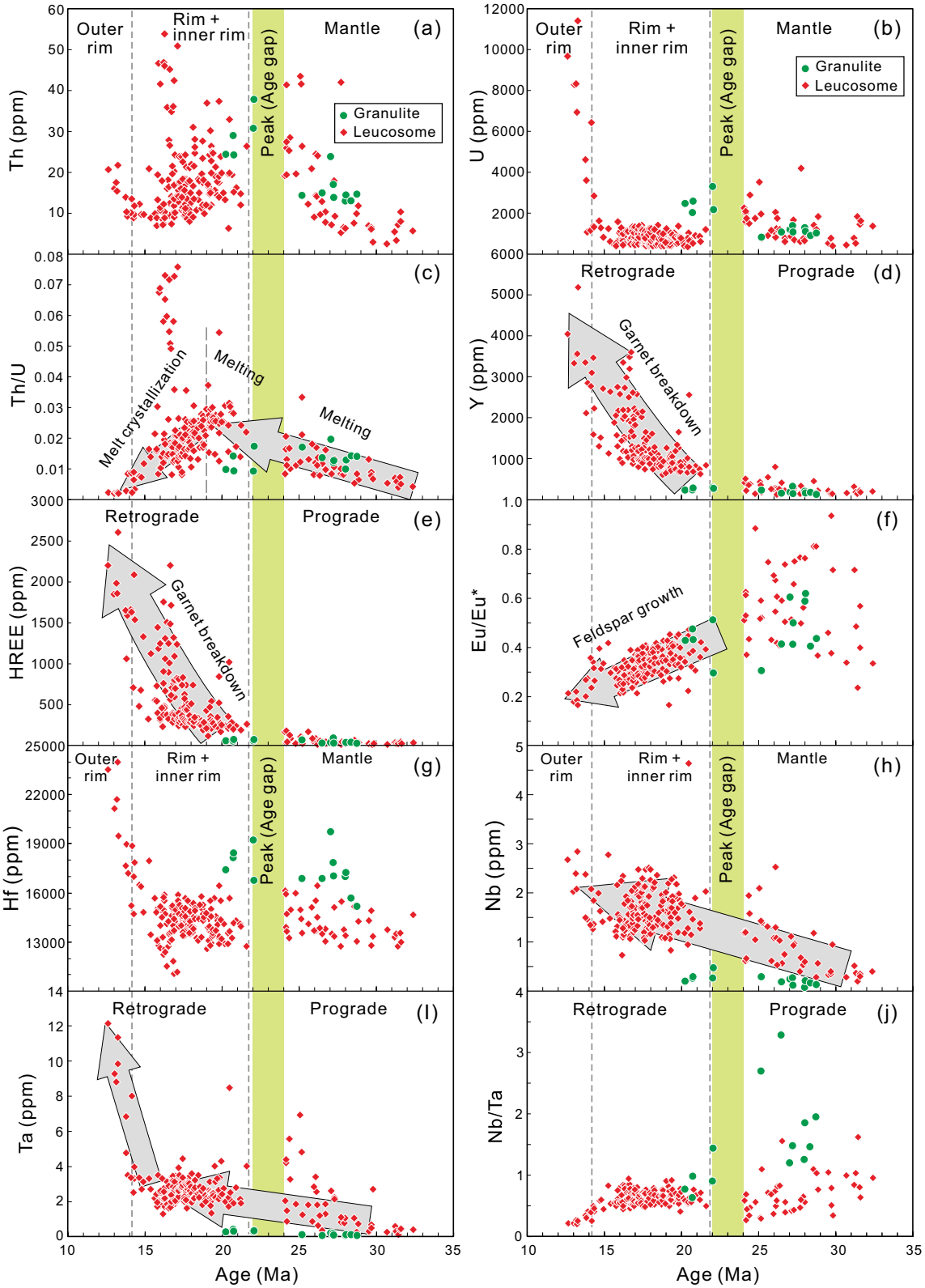
Outer rim
Rim + inner rim
Mantle
Peak (Age gap)
Granulite
Leucosome
(a)
Th (ppm)
(b)
U (ppm)
(c)
Th/U
Melt crystallization
Melting
Melting
(d)
Y (ppm)
Retrograde
Prograde
Garnet breakdown
(e)
HREE (ppm)
Garnet breakdown
(f)
Eu/Eu*
Feldspar growth
(g)
Hf (ppm)
(h)
Nb (ppm)
(I)
Ta (ppm)
(j)
Nb/Ta
Age (Ma)

Within the framework of chemical trends and ages of zircon (Figures 7–10), we make the following interpretations:

32–24 Ma (mantle domains): Increasing Th and Th/U (Figures 10a and 10c) indicate an increase in melt content. We interpret the slight increases in Y and HREE (Figures 10d and 10e) to reflect either diffusional re-equilibration of garnet (fluxing Y and HREE to the matrix), or slight garnet consumption.

24–22 Ma (age gap between mantles and rims): The increase in steepness of HREE patterns (Figures 7, 8, and 10e) across the age gap suggests garnet dissolution.

22–19 Ma (rim and inner rim): The increase in Th/U, slight increases in Y and HREE, and decrease in Eu/Eu* (Figures 10c–10f) indicate that melt fraction and plagioclase abundance were increasing, while garnet was dissolving.

19–14 Ma (rim and inner rim): The reversal in Th/U at ~19 Ma (Figure 10c) indicates a switch to crystallization of leucosomes, while the steepening slope for Y and HREE (Figures 10d and 10e) indicates an increasing rate of garnet consumption.

14–13 Ma (rim and outer rim): The offset for Eu/Eu* (Figure 10f) and the increased steepness of HREE and Y (Figures 10d and 10e) indicate further dissolution of garnet in the context of very late-stage feldspar growth and melt crystallization.

On the basis of the phase equilibrium modeling of Z. Zhang et al. (2017), we calculated isomodes of melt and minerals on a P-T pseudosection (Figures 11a–11e) as well as the dependence of the solidus temperature on the assumed amount of melt (e.g., to distinguish crystallization conditions of partially segregated leucosomes compared to the original melt-reintegrated composition; Figures 11f). In comparison with P-T diagrams contoured for isopleths of melt, garnet, and plagioclase (Figures 11a–11e), we can link the ages petrogenetically as follows:

Between 32 and 24 Ma, the increases in Th and Th/U (Figures 10a and 10c) indicate that zircon mantles formed during partial melting and increasing melt mode, likely through dissolution-reprecipitation or Ostwald ripening (Kohn & Kelly, 2018; Rubatto, 2017). The slight increase in Y and HREE with decreasing age (Figures 10d and 10e) is consistent with the formation of zircon at sufficiently high temperature for Y and HREE diffusion in garnet, or during a stage of very slight garnet dissolution. Phase equilibrium modeling indicates that the garnet mode slightly decreases and melt mode largely increases during prograde muscovite dehydration-melting (Figure 11c). Thus, we interpret the age of 32–24 Ma to represent the timing of prograde melting (Figure 11d).

The lack of zircon ages between 24 and 22 Ma does not allow close interpretation. However, zirconium mass-balance models show that the zircon mode should decrease during partial melting (Kelsey et al., 2008; Kelsey & Powell, 2011; Kohn et al., 2015; Yakymchuk et al., 2017). Therefore, we consider the 24–22 Ma age gap to bracket the timing of peak metamorphism and associated melting, when a large amount of melt formed over a relatively small change in pressure and temperature (Figure 11d).

Between 22 and 19 Ma, increases in Th, Th/U, HREE, and Y, and decrease in Eu/Eu* in zircon (Figures 10a and 10c–10f) are consistent with increases in melt and plagioclase fractions and a slight decrease in garnet fraction. These changes can occur only during a nearly isothermal decrease in pressure (Figures 11a–11e). Replacement of garnet and kyanite by sillimanite, biotite, and cordierite also requires a nearly isothermal decrease in pressure, so we infer high-temperature exhumation to retrograde pressures <6–7 kbar during this time interval. In the restitic granulite, we interpret the lack of large zircon domains younger than ~20–21 Ma (Figure 7a; Table S1), to reflect segregation of leucosomes. Leucosome segregation removes melt

Figure 10. Diagrams of composition versus age for key trace element values and ratios for zircon from the pelitic granulite and leucosomes. The data fields for zircon mantle, rim (and inner rim) and outer rim are demarcated by the dotted lines. The light green filled areas indicate the peak metamorphic age range (age gap). (a) Th, (b) U, (c) Th/U, (d) Y, (e) HREE, (f) Eu/Eu*, (g) Hf, (h) Nb, (i) Ta, and (j) Nb/Ta. Note that Th and Th/U increase distinctly in the zircon mantles, indicating an increasing melt content; Y and HREE increase and Eu/Eu* decrease markedly in the zircon rims, indicating garnet breakdown and feldspar growth during the partial melting and melt crystallization, respectively; Nb and Ta increase in variable degree from the zircon mantles to rims, and Nb/Ta shows variable, moderate and low ratios in the zircon mantles, rims + inner rims, and outer rims, respectively.

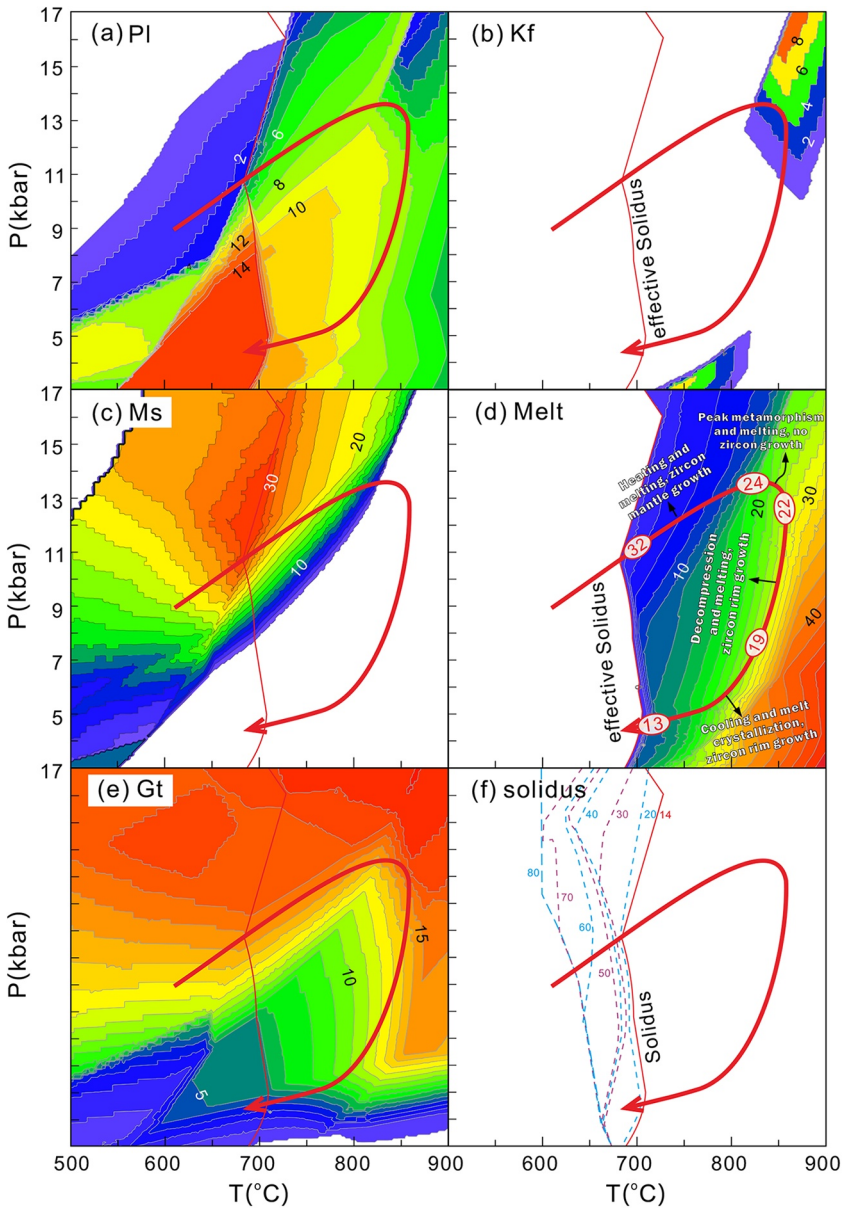

Figure 11. Isopleths of mineral and melt modes (white and black numbers, in volume percent) and the range of possible leucosome solidi, showing variations of major minerals and melt abundances along P-T evolution (bold red line with arrow; red numbers refer to metamorphic ages in Ma) and solidus temperature variation with different added melt volumes. The original melt-reintegrated solidus (effective solidus) is shown by thin red line. (a) Plagioclase increases slightly in abundance after crossing the solidus and during high-temperature exhumation, then increases rapidly during melt crystallization. (b) A small amount of K-feldspar is predicted at peak P-T conditions, but broke down during exhumation and cooling. (c) Muscovite decreases in abundance after the P-T path crosses the solidus, and completely disappears from the rock just before reaching peak metamorphic conditions. (d) Melt increases in abundance during prograde heating and nearly isothermal exhumation, then decreases during late-stage cooling. Labels along P-T-t path indicate periods of heating and melting, peak metamorphism and melting, decompression and melting, and cooling and melt crystallization as well as periods of zircon mantle and rim growth. The numbers marked on the P-T path refer to metamorphic ages in Ma. (e) Garnet does not change mode significantly after P-T path crosses the solidus, but decreases during exhumation and especially during cooling. (f) The solidus temperatures decrease with increasing melt content, and indicate that partially segregated leucosomes and zircons likely crystallized between ca. 650°C and ca. 700°C. The dotted lines represent solidi calculated using the melt-reintegrated bulk composition with different added melt volume, marked by the numbers (in wt%). Melt composition is from Z. Zhang et al. (2017).

as a major source of Zr, and decouples reaction of restitic garnet + biotite + sillimanite from feldspathic melt. However, segregation could not have happened instantaneously, and granulite and leucosomes could not have been completely chemically isolated (zircons from the granulite do have very thin rims). Possibly, segregation began earlier, even during the age gap at 22–24 Ma.

At ~19 Ma, the reversal in Th/U (Figure 10c) marks a major transition from melt generation to melt crystallization. The lack of thick rims of this age or younger in zircon from the restitic granulite (Figure 6a) suggests leucosome segregation was more complete by this time.

After 19 Ma, the steepening slope for Y and HREE (Figures 10d and 10e) indicates that the rate of garnet consumption increased during melt crystallization (decreasing Th/U). The large changes in slope of Y, HREE, and Eu/Eu* at 14–13 Ma (Figures 10d–10f) reflect rapid plagioclase growth and garnet breakdown during the latest stages of melt crystallization (Figures 11a and 11e). Segregation of leucosomes implies that the last zircon crystallization temperature (lowest solidus) could have been as low as ~650°C (Figure 11f).

7.2. Petrochronologically Informed Metamorphic P-T-t Path

Linking ages to our calculated mineral assemblage diagram is consistent with the following interpretation: prograde partial melting occurred with increasing P and T between 32 and 24 Ma up to peak P-T conditions of 825–850°C and ~13 kbar (Figures 5 and 11). A period of slight heating but substantial melt production at 24–22 Ma resulted in a hiatus of zircon growth or possibly caused zircon to dissolve. Exhumation to ca. 7 kbar and ~825°C occurred by 19 Ma, implying rapid exhumation (20 km in ~3 Myr, or ~6 mm/yr exhumation). Melts had likely segregated locally (Figure 3) by 19 Ma, and perhaps had started segregating as early as 22–24 Ma. The dramatically increasing Y and HREE in zircon to ~14 Ma are consistent with an increased rate of garnet dissolution along a quasi-isobaric cooling P-T path (Figure 11e). Zircon rims between 14 and 13 Ma represent the final crystallization of melts (Figure 11d).

These interpretations imply a ~20 Myr process of high-temperature metamorphism, melting, and melt crystallization. The prograde increases in P and T, and associated dehydration melting, began at least by ~32 Ma and lasted to ~24 Ma, the subsequent isothermal decompression melting occurred between ~22 Ma and 19 Ma, and late melt crystallization initiated at ~19 Ma and ended at ~13 Ma (Figure 11d). These interpretations are consistent with increasing recognition in the central and eastern Himalayan orogen of middle Eocene to Early Oligocene (45–30 Ma) high-grade metamorphism (e.g., Cottle, Searle, et al., 2009; Ding et al., 2016; Kellett et al., 2014; Kohn & Corrie, 2011; Lee & Whitehouse, 2007; Regis et al., 2014; Rubatto et al., 2013; Wang et al., 2015; Zhang et al., 2015; and many others) and leucogranite magmatism (e.g., Aikman et al., 2012, 2008; Gou et al., 2016; Hou et al., 2012; Liu et al., 2017; Wu et al., 2015; Zeng et al., 2011). The interpreted segregation of partial melts by 19 Ma and possibly as early as 22–24 Ma is consistent with older voluminous 18–23 Ma leucogranites exposed to the north at the STDS in the Yadong area (Gou et al., 2016; Liu et al., 2017) and in the upper GHS in neighboring Bhutan (Cooper et al., 2015; Kellett et al., 2009) and Sikkim (Kellett et al., 2013). The inferred ~3 Myr duration of rapid exhumation (between 22–19 Ma or ~6 mm/yr) of the granulite also generally agrees in age and tempo with the activity of the STDS and intra-GHS thrusts (especially the HHD) that are related to the extrusion of the GHS (see review of Carosi et al., 2018). Our interpretation supports previous studies that suggest that high-temperature ductile extension along the STDS lasted no more than a few million years at ~20 Ma (Carosi et al., 2013, 2018; Chambers et al., 2011; Iaccarino et al., 2017; Sachan et al., 2010), although other studies have proposed more protracted deformation, both earlier and later (see summary of Kellett et al., 2018).

7.3. Mechanisms of Melting of the Pelitic Granulite

Most studies of high-grade metamorphic rocks from the GHS demonstrate extensive partial melting to produce the Himalayan leucogranites (e.g., Aoya et al., 2005; Breton & Thompson, 1998; Guillot & Le Fort, 1995; Guo & Wilson, 2012; Harris et al., 1995; Harris & Massey, 1994; Knesel & Davidson, 2002; Le Fort et al., 1987; Patiño Douce & Harris, 1998; Weinberg, 2016; Zeng et al., 2012). Two distinct processes that lead to melting have been proposed: prograde heating with an increase in pressure (Groppo et al., 2010; Guilmette et al., 2011; Visonà & Lombardo, 2002; Zhang et al., 2004), and decompression melting during exhumation (Davidson et al., 1997; Guo & Wilson, 2012; Harris et al., 2004; Harris & Massey, 1994; Harrison

et al., 1997; Patiño Douce & Harris, 1998; Viskupic et al., 2005). Other studies have proposed water-fluxed melting (Gao et al., 2017; Gao & Zeng, 2014; Knesel & Davidson, 2002; Weinberg, 2016), but such melting occurs at much lower temperatures than we interpret for our rocks and is unlikely to be relevant to our study, an aqueous fluid is unstable at near-peak P-T conditions relative to melt, and all melts appear locally derived (Figure 3).

Migmatites in the GHS underwent granulite-facies metamorphism at 750°–850°C, which is sufficient to induce dehydration melting of muscovite and biotite during prograde heating of pelitic and felsic granulites, and to generate significant amounts of melt (up to 15–30 vol%) (Groppo et al., 2010, 2012; Guilmette et al., 2011; Rubatto et al., 2013; Zhang et al., 2015, Z. Zhang et al., 2017). Phase equilibria models show that during the prograde metamorphism of pelitic granulite, the volume of muscovite markedly decreases (Figure 11c), whereas the volume of melt distinctly increases (Figure 11d). Our peak P-T conditions as calculated based on the observed mineral assemblage imply that dehydration melting of muscovite during heating and burial produced melt volumes up to ~20 vol% (Figure 11d). Decreasing pressure would drive further melting if leucosomes maintain any communication with granulite (melt isopleths show comparable slopes for all models in Figure 11f), but the constraint that plagioclase must be increasing in abundance (Figure 11a) implies that total melt production did not exceed ~30 vol.% (Figure 11d), which is the amount we now observe as leucosomes in outcrop (Figure 3). Overall, prograde heating (and burial) drove most melt production of the pelitic granulite, whereas decompression drove subsidiary melting.

Many studies cite much lower melt volumes (≤10%) as a critical threshold for melt interconnectivity (Rosenberg & Handy, 2005) and escape (Brown, 2007, 2010; Etheridge et al., 2020). Interconnected melts are not necessarily mobile, however, and image processing of migmatites with incipient melt segregation (e.g., Figure 3; Figure 5 of Brown, 2010) indicates much higher melt volumes of c. 30% before segregation begins. Such a high fraction is consistent with mixed crystal-melt models, which indicate a high probability of melt extraction only at melt fractions >30% (Dufek & Bachmann, 2010). Whereas ~30% melt in the studied migmatites did not escape at the outcrop scale, the GHS consists mainly of anatectic pelitic and felsic granulites. More efficient melt extraction in other rocks, for example, because of lower viscosities (higher water content), higher melt fractions (higher primary mica contents, higher temperatures), structural idiosyncrasies (deformation and proximity to shear zones), and so on, could readily have sourced Himalayan leucogranites that occur in the upper structural level of the GHS and within the THS (see also Le Fort et al., 1987; Harris and Massey, 1994; Guillot & Le Fort, 1995; Harris et al., 1995; Groppo et al., 2013; Searle & Fryer, 1986; Searle, 2013; Wu et al., 2015; Zhang et al., 2015).

7.4. Tectonic Implications

7.4.1. Exhumation Mechanisms of the GHS

Despite several decades of investigations, exhumation mechanisms of the GHS remain vigorously debated. A major outstanding question focuses on the causal relationship between exhumation and partial melting. Many workers have argued that rapid decompression during exhumation resulted in the partial melting of the GHS, that is, that tectonics drove melting (e.g., Harris & Massey, 1994; Harrison et al., 1997; Zhang et al., 2004). However, recent studies (Ding et al., 2021; Iaccarino et al., 2015; Rubatto et al., 2013; Wang et al., 2015, 2016; Zhang et al., 2015; Z. M. Zhang et al., 2017) and this work reveals that the GHS underwent protracted (~10–20 Myr) high-temperature metamorphism and anatexis via dehydration melting from the Early Oligocene to Early Miocene (Figure 11). These ages distinctly precede the widely accepted Miocene timing of decompression melting (e.g., Harris et al., 2004). Partial melts dramatically reduce the strength and density of anatectic rocks (Rosenberg & Handy, 2005), so once melt contents reach a critical threshold, deformation must partition differently. We propose that the early (>25 Ma) melt generated during prograde metamorphism of the GHS was insufficient to promote significant changes to deformational style until it reached a critical threshold of at least 20 vol % (Figure 11d). At that point, either buoyancy forces triggered rapid exhumation of GHS rocks, or sufficient melt escaped from other GHS rocks to change the overall strength profile of the orogenic wedge. As Brown (2007, 2010) emphasizes, melt extraction simultaneously strengthens the lower crust (loss of inviscid liquid) and the upper crust (crystallization of strong, feldspar-rich rocks). According to critical wedge theory, a stronger wedge adopts a narrower taper, which could be achieved through activation of STDS extension. That is, melt extraction to form leucogranites could have

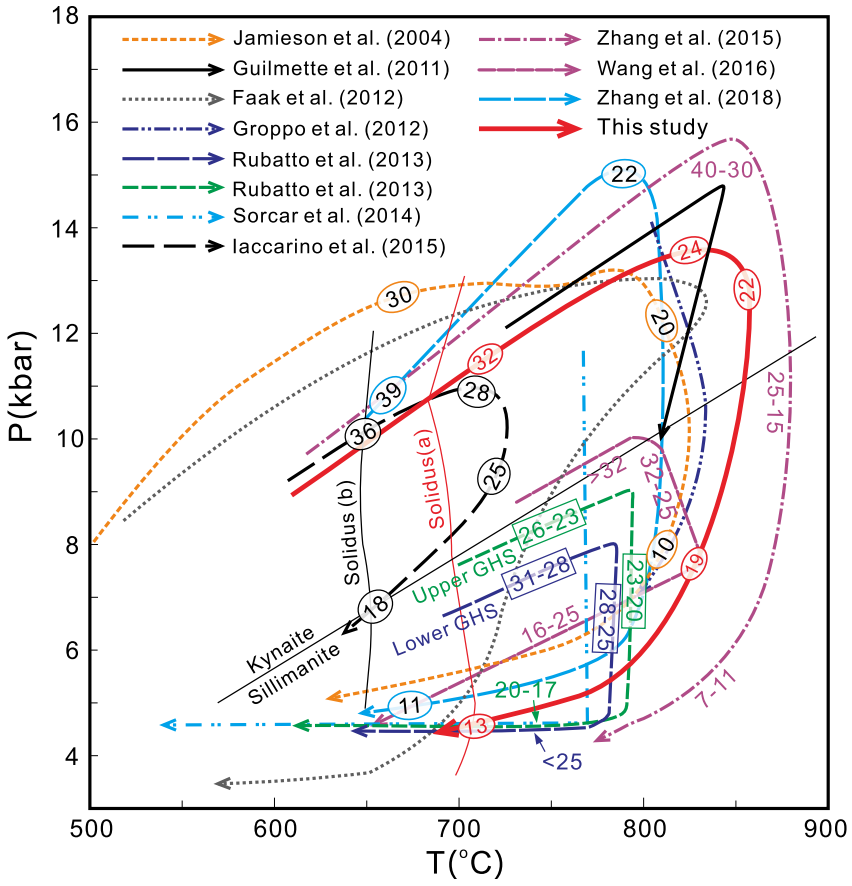

Figure 12. Metamorphic P-T-t path of the migmatitic pelitic granulite (this study) and published P-T (-t) paths for comparison. Published paths include pelitic and mafic granulites from the Sikkim region (Faak et al., 2012; Rubatto et al., 2013; Sorcar et al., 2014), felsic granulites from Nepal (Groppo et al., 2012; Iaccarino et al., 2015) and Namche Barwa (Guilmette et al., 2011), pelitic granulites from Nyalam (Wang et al., 2016) and Namche Barwa (Zhang et al., 2015), mafic granulite from Namche Barwa (Zhang et al., 2018), and channel flow model (Jamieson et al., 2004). All the numbers marked on P-T path refer to metamorphic ages in Ma. The solidus (a) and solidus (b) are after this study and Iaccarino et al. (2015), respectively.

catalyzed STDS extension by strengthening the wedge. Once exhumation began, decompression melting provided a positive feedback to continue driving exhumation. That is, melting catalyzed initial exhumation that then augmented further melting and exhumation.

7.4.2. Comparisons to P-T-t Paths From the Eastern and Central Himalaya

Many studies infer clockwise P-T paths of the GHS rocks in the eastern Himalaya, but have reported distinctly different metamorphic P-T conditions, depending on geographic area and structural level (Figure 12). Some previous studies could have underestimated peak-pressure conditions in metapelites because late-stage sillimanite- and cordierite-bearing low-pressure (LP) assemblages commonly overprint prograde assemblages (e.g., Groppo et al., 2009, 2010, 2012; Harris et al., 2004; Iaccarino et al., 2015; Wang et al., 2016; Zhang et al., 2015; Z. Zhang et al., 2017). At least in some rocks, prograde assemblages contained kyanite plus melt and were stable only at $P > 10$ kbar and $T \geq 800$°C.

In the Sikkim and Yadong region, calculated peak metamorphic pressures of migmatitic granulites of the GHS are particularly different among different studies. Some studies report pressures of at most 8–10 kbar at ~800°C and assign these rocks to a medium-pressure (MP) metamorphic belt characterized by sillimanite–K-feldspar ± cordierite assemblages (Anczkiewicz et al., 2014; Dasgupta et al., 2004, 2009; Gaidies

et al., 2015; Rubatto et al., 2013). In contrast, other studies argued that the GHS in Sikkim formed at pressures of 13–15 kbar, indicating high-pressure granulite-facies metamorphism within the kyanite stability field; it was only subsequent decompression at an elevated temperature that caused rocks to enter the sillimanite stability field to produce medium-pressure assemblages (Harris et al., 2004; Sorcar et al., 2014; Z. Zhang et al., 2017).

Pressures calculated for rocks approximately along strike from ours in Sikkim (Figure 1b) are approximately 4 kbar lower than ours (8–9 kbar at ~800°C; Figure 12; Rubatto et al., 2013). These disparities could reflect different structural levels and imperfect structural correlation. Nonetheless, a high-pressure metamorphic stage up to 12–13 kbar also has been estimated for mafic granulites occurring as blocks within pelitic and felsic granulites in the Sikkim area (Figure 12; Faak et al., 2012), as well as higher metamorphic pressures up to 14–20 kbar for granulitized eclogites in neighboring regions of Nepal and Bhutan (Corrie et al., 2010; Cottle, Jessup, et al., 2009; Groppo et al., 2007; Grujic et al., 2011; Kellett et al., 2014; Li et al., 2019; Lombardo & Rolfo, 2000; Wang et al., 2017; Warren et al., 2011). Recent studies have indicated that the GHS anatectic granulites in the eastern Himalaya commonly experienced high-pressure granulite-facies metamorphism with P-T conditions of up to 12–16 kbar and clockwise P-T paths (e.g., Ding et al., 2001; Groppo et al., 2012, 2010; Guilmette et al., 2011; Kali et al., 2010; Tian et al., 2016; Zhang et al., 2015, 2018; Z. M. Zhang et al., 2010). Thus, our inferred peak P-T condition and P-T path are consistent with numerous studies both nearby in Sikkim and more generally within the eastern sector of the Himalaya.

7.4.3. Architecture of the GHS

Most petrochronological studies imply that different GHS rocks witnessed significantly different initiation and duration of high-temperature metamorphism and melting (e.g., cf. Figure 12), and that several tectonometamorphic discontinuities occur within the GHS (e.g., Carosi et al., 2010; Corrie & Kohn, 2011; Grujic et al., 2011; Kohn et al., 2004; Imayama et al., 2012; Larson et al., 2013; Montomoli et al., 2013; Larson & Cottle, 2014; Wang et al., 2013, 2015, 2016; Warren et al., 2011, 2014). If so, the GHS should have a complex architecture (Goscombe et al., 2006; Larson et al., 2015; Montomoli et al., 2015; Mukherjee, 2015; Wang et al., 2016) that contrasts to older models in which the GHS forms a single coherent tectonic unit with only two structures, the STD and MCT, as its top and bottom boundaries (e.g., Le Fort, 1975; Searle et al., 2011; Yin & Harrison, 2000). In the Sikkim Himalaya, based on zircon and monazite petrochronological study of the pelitic granulites, Rubatto et al. (2013) and Anczkiewicz et al. (2014) argued for at least two slices of GHS rocks, each with a distinct P-T-t history, separated by an out-of-sequence tectonometamorphic discontinuity (the Zema Fault, ZF; Figure 1b). In their interpretation, the lower GHS reached peak metamorphism and began melting earlier than the upper GHS (Figure 12). It is evident, however, that the P-T-t path of the granulite in this study differs markedly from either the upper or lower GHS rocks examined in Rubatto et al. (2013), despite their mutual proximity. In addition, Chakraborty et al. (2019) proposed that the structurally lower CTT (HHD, Figures 1b and 2) initiated ca. 27 Ma (based on interpretations of Rubatto et al., 2013), before the peak age (ca. 24–22 Ma) of our samples. Because the hanging wall of a thrust should cool, not heat, during thrusting, these ages are not easily reconcilable. Either there are more tectonometamorphic discontinuities in the area, discontinuities in the Sikkim area do not propagate into the adjacent Yadong area, or the ages of CTT movement and Sikkim metamorphism should be reconsidered. As one example, acknowledging that Eu trends for Sikkim rocks at low structural levels have interpretational latitude, the ages and inferred P-T-t path there can be reconciled with the younger peak metamorphic age (22–24 Ma) that we infer at Yadong and with younger CTT movement.

For Nepal and nearby areas, where there has been more work on tectonometamorphic discontinuities in the GHS, different studies yield diverse interpretations of the numbers of thrust sheets and prograde metamorphic ages. Many petrochronological studies divide the GHS into two or more thrust sheets, with decreasing metamorphic conditions and ages toward the lower structural levels (Corrie & Kohn, 2011; Larson et al., 2013; Montomoli et al., 2013; Walters & Kohn, 2017; Wang et al., 2015, 2016). Other studies (Ambrose et al., 2015; Goscombe et al., 2018; Larson et al., 2015) have proposed that the GHS contains a series of slabs with wide-ranging metamorphic conditions and ages. In the lower GHS of the Kali Gandaki valley, central Nepal, ages are interpreted to reflect prograde metamorphism and protracted high-pressure melting

between 36 and 28 Ma, with high-temperature decompression and cooling between 25 and 18 Ma (Carosi et al., 2014; Iaccarino et al., 2015; Figure 12). These metamorphic and anatectic ages are distinctly older than those obtained from the lower GHS in other studies, so in a broader geographic context appear incompatible with the decreasing metamorphic age trend toward lower structural levels of the GHS as suggested in many studies.

The conflicting interpretations regarding the number of thrust sheets and the timing of their metamorphism across Nepal-Sikkim sector of the Himalaya, may perhaps, in part, reflect an artifact arising through reliance on geochronologic analysis of the residuum of migmatites. The studied Yadong rocks clearly show that the zircon from the pelitic granulite records only the timescale of prograde metamorphism and associated partial melting, whereas zircon from the leucosomes provides a more nearly complete picture of the metamorphism, anatexis, and melt crystallization. Some prior studies restricted consideration to specific rock types that may not have recorded the full history of anatexis and high-temperature exhumation. If so, the spatial distribution and temporal evolution of tectonometamorphic discontinuities within the GHS may be more coherent than currently appear along different sectors of the Himalaya. This hypothesis could be tested by analyzing leucosomes in addition to melanosomes in future study.

7.4.4. Compatibility With Numerical Models

Several different thermal-mechanical and thermal-kinematic models have been proposed for the Himalaya, including channel flow (Beaumont et al., 2004; Godin et al., 2006; Jamieson et al., 2004), critical taper-type models (Célérier et al., 2009; Herman et al., 2010), and generalized thermal-mechanical models of continental collision (e.g., Warren et al., 2008). Channel flow has commonly been proposed as a mechanism to explain the tectonics, P-T paths, and timing of metamorphism and partial melting for the Himalayan orogen. Application of such models to the GHS, especially channel flow does successfully reproduce the shape of many P-T paths observed across the eastern Himalaya (Jamieson et al., 2004), including the prograde heating and isothermal decompression that characterizes the GHS granulites from Yadong (Figures 11 and 12). However, the rates of exhumation are quite different (Figure 11), for example, requiring more than 10 Myr for pressure to decrease by 4–5 kbar in channel flow models, whereas our data indicate ca. 5.5 kbar decompression in only 3 Myr. As identified first by Jamieson et al. (2004), the timing of cooling and exhumation of the GHS is also much earlier than channel flow models predict. Although we do not have sufficient data to completely evaluate thermal-mechanical and thermal-kinematic models proposed for the Himalayan orogen, the improved timescales of metamorphism and exhumation for the GHS now call for more sophisticated numerical simulations that better explain natural petrochronological constraints. Future models should account not only for melt weakening (Beaumont et al, 2001, 2004; Jamieson et al., 2004), but also strengthening associated with melt extraction (Brown, 2007, 2010).

8. Conclusions

The migmatitic pelitic granulite of the GHS in the Yadong area, eastern Himalaya, underwent high-temperature and high-pressure granulite-facies metamorphism and associated dehydration melting. Zircon from the pelitic granulite and leucosomes has variable ages ranging from 32 Ma to 13 Ma with an age gap between 24 Ma and 22 Ma, while Y, Th, U, Hf, Nb, Ta, and HREE, Th/U, Eu/Eu*, and Nb/Ta of zircon show systematic changes over time. These changes of trace element concentrations and ratios can be linked to important reactions involving melt, garnet, and plagioclase, allowing rates of melting, isothermal exhumation, and melt crystallization to be determined. The high-temperature metamorphism, partial melting, and melt crystallization process of the granulite was over ~20 Myr: initial heating above the solidus (~700°C) by ~32 Ma until ~24 Ma, isothermal decompression melting between ~22 Ma and 19 Ma, and melt crystallization between ~19 Ma and ~13 Ma. The intensive melting and progressive increase in melt abundance in the region between 24 and 19 Ma could have triggered the exhumation of GHS rocks, and contributed to the formation of Himalayan leucogranites. Future study should test tectonometamorphic discontinuities within the GHS and the implications for complex internal architecture through a more comprehensive chronologic analysis of both granulites and leucosomes.

Data Availability Statement

Supporting information presented as part of this study is available from the Figshare Repository (https://doi.org/10.6084/m9.figshare.13185278).

Acknowledgments
The authors thank Editor W. Behr, AE G. Fellin, K. Larson, and an anonymous reviewer for meticulous and insightful reviews. This study was co-supported by the National Natural Science Foundation of China (Grant nos. 91855210, 41872064, 41802071, and 41602062), the National Key Research and Development Project of China (Grant no. 2016YFC0600310), the U.S. National Science Foundation (Grant nos. EAR1450507, OIA1545903, and EAR1918488), Fundamental Research Funds for the Central Universities of China (Grant no. 649911026), and the China Geological Survey (Grant no. DD20160201).

References

Aikman, A. B., Harrison, T. M., & Hermann, J. (2012). Age and thermal history of Eo- and Neohimalayan granitoids, eastern Himalaya. *Journal of Asian Earth Sciences*, *51*, 85–97. https://doi.org/10.1016/j.jseaes.2012.01.011

Aikman, A. B., Harrison, T. M., & Lin, D. (2008). Evidence for early (>44 Ma) Himalayan crustal thickening, Tethyan Himalaya, southeastern Tibet. *Earth and Planetary Science Letters*, *274*(1–2), 14–23. https://doi.org/10.1016/j.epsl.2008.06.038

Ambrose, T. K., Larson, K. P., Guilmette, C., Cottle, J. M., Buckingham, H., & Rai, S. (2015). Lateral extrusion, underplating, and out-of-sequence thrusting within the Himalayan metamorphic core, Kanchenjunga, Nepal. *Lithosphere*, *7*(4), 441–464. https://doi.org/10.1130/L437.1

Anczkiewicz, R., Chakraborty, S., Dasgupta, S., Mukhopadhyay, D., & Kołtonik, K. (2014). Timing, duration and inversion of prograde Barrovian metamorphism constrained by high resolution Lu-Hf garnet dating: A case study from the Sikkim Himalaya, NE India. *Earth and Planetary Science Letters*, *407*, 70–81. https://doi.org/10.1016/j.epsl.2014.09.035

Aoya, M., Wallis, S. R., Terada, K., Lee, J., Kawakami, T., Wang, Y., & Heizler, M. (2005). North-south extension in the Tibetan crust triggered by granite emplacement. *Geology*, *33*(11), 853–856. https://doi.org/10.1130/G21806.1

Beaumont, C., Jamieson, R. A., Nguyen, M. H., & Lee, B. (2001). Himalayan tectonics explained by extrusion of a low-viscosity crustal channel coupled to focused surface denudation. *Nature*, *414*, 738–742. https://doi.org/10.1038/414738a

Beaumont, C., Jamieson, R. A., Nguyen, M. H., & Medvedev, S. (2004). Crustal channel flows: 1. Numerical models with applications to the tectonics of the Himalayan-Tibetan orogen. *Journal of Geophysical Research*, *109*, B06406. https://doi.org/10.1029/2003JB002809

Breton, N. L., & Thompson, A. B. (1998). Fluid-absent (dehydration) melting of biotite in metapelites in the early stages of crustal anatexis. *Contributions to Mineralogy and Petrology*, *99*(2), 226–237. https://doi.org/10.1007/BF00371463

Brown, M. (2007). Crustal melting and melt extraction, ascent and emplacement in orogens: Mechanisms and consequences. *Journal of the Geological Society*, *164*(4), 709–730. http://dx.doi.org/10.1144/0016-76492006-171

Brown, M. (2010). Melting of the continental crust during orogenesis: The thermal, rheological, and compositional consequences of melt transport from lower to upper continental crust. *Canadian Journal of Earth Sciences*, *47*, 655–694. https://doi.org/10.1139/e09-057

Brown, M., Averkin, Y. A., McLellan, E. L., & Sawyer, E. W. (1995). Melt segregation in migmatites. *Journal of Geophysical Research*, *100*(B8), 15655–15679. https://doi.org/10.1029/95JB00517

Carlson, W. D. (2012). Rates and mechanism of Y, REE, and Cr diffusion in garnet. *American Mineralogist*, *97*, 1598–1618. https://doi.org/10.2138/am.2012.4108

Carosi, R., Gemignani, L., Godin, L., Iaccarino, S., Larson, K., Montomoli, C., & Rai, S. M. (2014). A geological journey through the deepest gorge on Earth: The Kali Gandaki valley section, central Nepal. *Journal of the Virtual Explorer*, *47*, 7. https://doi.org/10.3809/Jvirtex.vol.2014.052

Carosi, R., Montomoli, C., Iaccarino, S., & Visona, D. (2018). *Structural evolution, metamorphism and melting in the Greater Himalayan Sequence in central-western Nepal*. In P. J. Treloar, & M. P. Searle (Eds.), Himalayan tectonics: A modern synthesis (Vol. *483*, pp. 305–323). London: Geological Society Special Publications. https://doi.org/10.1144/SP483.3

Carosi, R., Montomoli, C., Rubatto, D., & Visonà, D. (2010). Late Oligocene high-temperature shear zones in the core of the Higher Himalayan Crystallines (Lower Dolpo, western Nepal). *Tectonics*, *29*, TC4029. https://doi.org/10.1029/2008TC002400

Carosi, R., Montomoli, C., Rubatto, D., & Visonà, D. (2013). Leucogranite intruding the South Tibetan Detachment in western Nepal: Implications for exhumation models in the Himalayas. *Terra Nova*, *25*(6), 478–489. https://doi.org/10.1111/ter.12062

Catlos, E. J., Dubey, C. S., Harrison, T. M., & Edwards, M. A. (2004). Late Miocene movement within the Himalayan Main Central Thrust shear zone, Sikkim, north-east India. *Journal of Metamorphic Geology*, *22*, 207–226. https://doi.org/10.1111/j.1525-1314.2004.00509.x

Célérier, J., Harrison, T. M., Beyssac, O., Herman, F., Dunlap, W. J., & Webb, A. A. G. (2009). The Kumaun and Garwhal Lesser Himalaya, India: Part 2. Thermal and deformation histories. The *Geological Society of America Bulletin*, *121*(9–10), 1281–1297. https://doi.org/10.1130/B26343.1

Chakraborty, S., Anczkiewicz, R., Gaidies, F., Rubatto, D., Sorcar, N., Faak, K., et al. (2016). A review of thermal history and timescales of Tectonometamorphic processes in Sikkim Himalaya (NE India) and implications for rates of metamorphic processes. *Journal of Metamorphic Geology*, *34*(8), 785–803. https://doi.org/10.1111/jmg.12200

Chakraborty, S., Mukhopadhyay, D. K., Chowdhury, P., Rubatto, D., Anczkiewicz, R., Trepmann, C., et al. (2017). Channel flow and localized fault bounded slice tectonics (LFBST): Insights from petrological, structural, geochronological and geospeedometric studies in the Sikkim Himalaya, NE India. *Lithos*, *282–283*, 464–482. https://doi.org/10.1016/j.lithos.2017.01.024

Chakraborty, S., Mukul, M., Mathew, G., & Pande, K. (2019). Major shear zone within the Greater Himalayan Sequence and sequential evolution of the metamorphic core in Sikkim, India. *Tectonophysics*, *770*, 228183. https://doi.org/10.1016/j.tecto.2019.228183

Chambers, J., Parrish, R., Argles, T., Harris, N., & Horstwood, M. (2011). A short duration pulse of ductile normal shear on the outer South Tibetan detachment in Bhutan: Alternating channel flow and critical taper mechanics of the eastern Himalaya. *Tectonics*, *30*(2). TC2005. https://doi.org/10.1029/2010TC002784

Colchen, M., Le Fort, P., & Pecher, A. (1986). *Recherches geologiques dans l'Himalaya du Nepal, Annapurna; Manaslu, Ganesh Himal; notice de la carte geologique au 1/200 000 —Geological research in the Nepal Himalayas, Annapurna, Manaslu, Ganesh Himal; 1:20,000 geological map*.

Cooper, F. J., Hodges, K. V., Parrish, R. R., Roberts, N. M. W., & Horstwood, M. S. A. (2015). Synchronous N-S and E-W extension at the Tibet-to-Himalaya transition in NW Bhutan. *Tectonics*, *34*(7), 1375–1395. https://doi.org/10.1002/2014TC003712

Corrie, S. L., & Kohn, M. J. (2011). Metamorphic history of the central Himalaya, Annapurna region, Nepal, and implications for tectonic models. *The Geological Society of America Bulletin*, *123*(9–10), 1863–1879. https://doi.org/10.1130/B30376.1

Corrie, S. L., Kohn, M. J., & Vervoort, J. D. (2010). Young eclogite from the Greater Himalayan Sequence, Arun Valley, eastern Nepal: P-T-t path and tectonic implications. *Earth and Planetary Science Letters*, *289*(3), 406–416. https://doi.org/10.1016/j.epsl.2009.11.029

Cottle, J. M., Larson, K. P., & Kellett, D. A. (2015). How does the mid-crust accommodate deformation in large, hot collisional orogens? A review of recent research in the Himalayan orogen. *Journal of Structural Geology*, *78*, 119–133. https://doi.org/10.1016/j.jsg.2015.06.008

Cottle, J. M., Jessup, M. J., Newell, D. L., Horstwood, M. S. A., Noble, S. R., Parrish, R. R., et al. (2009). Geochronology of granulitized eclogite from the Ama Drime Massif: Implications for the tectonic evolution of the South Tibetan Himalaya. *Tectonics*, *28*(1). TC1002. https://doi.org/10.1029/2008TC002256

Cottle, J. M., Jessup, M. J., Newell, D. L., Searle, M. P., Law, R. D., & Horstwood, M. S. A. (2007). Structural insights into the early stages of exhumation along an orogen-scale detachment: The South Tibetan Detachment System, Dzakaa Chu section, Eastern Himalaya. *Journal of Structural Geology*, *29*(11), 1781–1797. https://doi.org/10.1016/j.jsg.2007.08.007

Cottle, J. M., Searle, M. P., Horstwood, M. S. A., & Waters, D. J. (2009). Timing of midcrustal metamorphism, melting, and deformation in the Mount Everest Region of Southern Tibet revealed by U(-Th)-Pb geochronology. *The Journal of Geology*, *117*(6), 643–664. https://doi.org/10.1086/605994

Dasgupta, S., Chakraborty, S., & Neogi, S. (2009). Petrology of an inverted Barrovian sequence of metapelites in Sikkim Himalaya, India: Constraints on the tectonics of inversion. *American Journal of Science*, *309*(1), 43–84. http://dx.doi.org/10.2475/01.2009.02

Dasgupta, S., Ganguly, J., & Neogi, S. (2004). Inverted metamorphic sequence in the Sikkim Himalayas: Crystallization history, P-T gradient and implications. *Journal of Metamorphic Geology*, *22*(5), 395–412. https://doi.org/10.1111/j.1525-1314.2004.00522.x

Davidson, C., Grujic, D. E., Hollister, L. S., & Schmid, S. M. (1997). Metamorphic reactions related to decompression and synkinematic intrusion of leucogranite, High Himalayan Crystallines, Bhutan. *Journal of Metamorphic Geology*, *15*(5), 593–612. https://doi.org/10.1111/j.1525-1314.1997.tb00638.x

Ding, H., Kohn, M. J., & Zhang, Z. (2021). Long-lived (ca. 22-24 Myr) partial melts in the eastern Himalaya: Petrochronologic constraints and tectonic implications. *Earth and Planetary Science Letters*, *558*, 116764. https://doi.org/10.1016/j.epsl.2021.116764

Ding, H., Zhang, Z., Dong, X., Tian, Z., Xiang, H., Mu, H., et al. (2016). Early Eocene (c . 50 Ma) collision of the Indian and Asian continents: Constraints from the North Himalayan metamorphic rocks, southeastern Tibet. *Earth and Planetary Science Letters*, *435*, 64–73. https://doi.org/10.1016/j.epsl.2015.12.006

Ding, L., Zhong, D., Yin, A., Kapp, P., & Harrison, T. M. (2001). Cenozoic structural and metamorphic evolution of the eastern Himalayan syntaxis (Namche Barwa). *Earth and Planetary Science Letters*, *192*(3), 423–438. https://doi.org/10.1016/S0012-821X(01)00463-0

Dufek, J., & Bachmann, O. (2010). Quantum magmatism: Magmatic compositional gaps generated by melt-crystal dynamics. *Geology*, *38*(8), 687–690. https://doi.org/10.1130/G30831.1

Engi, M., Lanari, P., & Kohn, M. J. (2017). Significant ages—An introduction to petrochronology. *Reviews in Mineralogy and Geochemistry*, *83*(1), 1–12. https://doi.org/10.2138/rmg.2017.83.1

Etheridge, M. A., Daczko, N. R., Chapman, T., & Stuart, C. A. (2020). Mechanisms of melt extraction during lower crustal partial melting. *Journal of Metamorphic Geology*, *39*(1), 57–75. https://doi.org/10.1111/jmg.12561

Faak, K., Chakraborty, S., & Dasgupta, S. (2012). Petrology and tectonic significance of metabasite slivers in the Lesser and Higher Himalayan domains of Sikkim, India. *Journal of Metamorphic Geology*, *30*(6), 599–622. https://doi.org/10.1111/j.1525-1314.2012.00987.x

Gaidies, F., Petley-Ragan, A., Chakraborty, S., Dasgupta, S., & Jones, P. (2015). Constraining the conditions of Barrovian metamorphism in Sikkim, India: P-T-t paths of garnet crystallization in the Lesser Himalayan Belt. *Journal of Metamorphic Geology*, *33*(1), 23–44. https://doi.org/10.1111/jmg.12108

Gao, L.-E., & Zeng, L. (2014). Fluxed melting of metapelite and the formation of Miocene high-CaO two-mica granites in the Malashan gneiss dome, southern Tibet. *Geochimica et Cosmochimica Acta*, *130*, 136–155. https://doi.org/10.1016/j.gca.2014.01.003

Gao, L.-E., Zeng, L., & Asimow, P. D. (2017). Contrasting geochemical signatures of fluid-absent versus fluid-fluxed melting of muscovite in metasedimentary sources: The Himalayan leucogranites. *Geology*, *45*(1), 39–42. https://doi.org/10.1130/G38336.1

Godin, L., Grujic, D., Law, R. D., & Searle, M. P. (2006). *Channel flow, ductile extrusion and exhumation in continental collision zones: An introduction*. In R. D. Law, et al. (Eds.), channel flow, ductile extrusion and exhumation in continental collision zones (Vol. *268*, pp. 1–23). Geological Society of London, Special Publication. http://dx.doi.org/10.1144/GSL.SP.2006.268.01.01

Goscombe, B., Gray, D., & Foster, D. A. (2018). Metamorphic response to collision in the Central Himalayan orogen. *Gondwana Research*, *57*, 191–265. https://doi.org/10.1016/j.gr.2018.02.002

Goscombe, B., Gray, D., & Hand, M. (2006). Crustal architecture of the Himalayan metamorphic front in eastern Nepal. *Gondwana Research*, *10*(3–4), 232–255. https://doi.org/10.1016/j.gr.2006.05.003

Gou, Z. B., Zhang, Z., Dong, X., Xiang, H., Ding, H., Tian, Z., & Lei, H. (2016). Petrogenesis and tectonic implications of the Yadong leucogranites, southern Himalaya. *Lithos*, *256–257*, 300–310. https://doi.org/10.1016/j.lithos.2016.04.009

Gou, Z. B., Zhang, Z. M., Dong, X., Ding, H. X., Xiang, H., Lei, H. C., et al. (2015). Petrogenesis and tectonic significance of the Early Paleozoic granitic gneisses from the Yadong area, southern Tibet. *Acta Petrologica Sinica*, *31*(12), 3674–3686.

Groppo, C., Lombardo, B., Rolfo, F., & Pertusati, P. (2007). Clockwise exhumation path of granulitized eclogites from the Ama Drime range (Eastern Himalayas). *Journal of Metamorphic Geology*, *25*(1), 51–75. https://doi.org/10.1111/j.1525-1314.2006.00678.x

Groppo, C., Rolfo, F., & Indares, A. (2012). Partial melting in the higher Himalayan crystallines of Eastern Nepal: The effect of decompression and implications for the 'Channel Flow' Model. *Journal of Petrology*, *53*(5), 1057–1088. https://doi.org/10.1093/petrology/egs009

Groppo, C., Rolfo, F., & Lombardo, B. (2009). P-T evolution across the Main Central Thrust Zone (Eastern Nepal): Hidden discontinuities revealed by petrology. *Journal of Petrology*, *50*(6), 1149–1180. https://doi.org/10.1093/petrology/egp036

Groppo, C., Rolfo, F., & Mosca, P. (2013). The cordierite-bearing anatectic rocks of the higher Himalayan crystallines (eastern Nepal): Low-pressure anatexis, melt productivity, melt loss and the preservation of cordierite. *Journal of Metamorphic Geology*, *31*(2), 187–204. https://doi.org/10.1111/jmg.12014

Groppo, C., Rubatto, D., Rolfo, F., & Lombardo, B. (2010). Early Oligocene partial melting in the Main Central Thrust Zone (Arun valley, eastern Nepal Himalaya). *Lithos*, *118*(3), 287–301. https://doi.org/10.1016/j.lithos.2010.05.003

Grujic, D., Warren, C. J., & Wooden, J. L. (2011). Rapid synconvergent exhumation of Miocene-aged lower orogenic crust in the eastern Himalaya. *Lithosphere*, *3*(5), 346–366. https://doi.org/10.1130/L154.1

Guillot, S., & Le Fort, P. (1995). Geochemical constraints on the bimodal origin of High Himalayan leucogranites. *Lithos*, *35*(3), 221–234. https://doi.org/10.1016/0024-4937(94)00052-4

Guillot, S., Mahéo, G., de Sigoyer, J., Hattori, K. H., & Pêcher, A. (2008). Tethyan and Indian subduction viewed from the Himalayan high- to ultrahigh-pressure metamorphic rocks. *Tectonophysics*, *451*(1), 225–241. https://doi.org/10.1016/j.tecto.2007.11.059

Guilmette, C., Indares, A., & Hébert, R. (2011). High-pressure anatectic paragneisses from the Namche Barwa, Eastern Himalayan Syntaxis: Textural evidence for partial melting, phase equilibria modeling and tectonic implications. *Lithos*, *124*(1), 66–81. https://doi.org/10.1016/j.lithos.2010.09.003

Guo, Z., & Wilson, M. (2012). The Himalayan leucogranites: Constraints on the nature of their crustal source region and geodynamic setting. *Gondwana Research*, *22*(2), 360–376. https://doi.org/10.1016/j.gr.2011.07.027

Harris, N., Ayres, M., & Massey, J. (1995). Geochemistry of granitic melts produced during the incongruent melting of muscovite: Implications for the extraction of Himalayan leucogranite magmas. *Journal of Geophysical Research*, *100*, 15767–15777. https://doi.org/10.1029/94JB02623

Harris, N., & Massey, J. (1994). Decompression and anatexis of Himalayan metapelites. *Tectonics*, *13*(6), 1537–1546. https://doi.org/10.1029/94TC01611

Harris, N. B. W., Caddick, M., Kosler, J., Goswami, S., Vance, D., & Tindle, A. G. (2004). The pressure-temperature-time path of migmatites from the Sikkim Himalaya. *Journal of Metamorphic Geology*, *22*(3), 249–264. https://doi.org/10.1111/j.1525-1314.2004.00511.x

Harrison, T. M., Grove, M., Lovera, O. M., & Catlos, E. J. (1998). A model for the origin of Himalayan anatexis and inverted metamorphism. *Journal of Geophysical Research*, *103*, 27017–27032. https://doi.org/10.1029/98JB02468

Harrison, T. M., Lovera, O. M., & Grove, M. (1997). New insights into the origin of two contrasting Himalayan granite belts. *Geology*, *25*(10), 899–902. https://doi.org/10.1130/0091-7613(1997)025<0899:NIITOO>2.3.CO;2

Herman, F., Copeland, P., Avouac, J. P., Bollinger, L., Mahéo, G., Le Fort, P., et al. (2010). Exhumation, crustal deformation, and thermal structure of the Nepal Himalaya derived from the inversion of thermochronological and thermobarometric data and modeling of the topography. *Journal of Geophysical Research*, *115*(6), B06407. https://doi.org/10.1029/2008JB006126

Hermann, J. (2002). Allanite: Thorium and light rare earth element carrier in subducted crust. *Chemical Geology*, *192*(3–4), 289–306. https://doi.org/10.1016/S0009-2541(02)00222-X

Holder, R. M., Yakymchuk, C., & Viete, D. R. (2020). Accessory mineral Eu anomalies in suprasolidus rocks: Beyond feldspar. *Geochemistry, Geophysics, Geosystems*, *21*(8). e2020GC009052. https://doi.org/10.1029/2020GC009052

Hou, Z.-Q., Zheng, Y.-C., Zeng, L.-S., Gao, L.-E., Huang, K.-X., Li, W., et al. (2012). Eocene-Oligocene granitoids in southern Tibet: Constraints on crustal anatexis and tectonic evolution of the Himalayan orogen. *Earth and Planetary Science Letters*, *349–350*, 38–52. https://doi.org/10.1016/j.epsl.2012.06.030

Hu, Z., Zhang, W., Liu, Y., Gao, S., Li, M., Zong, K., et al. (2015). "Wave" signal-smoothing and mercury-removing device for laser ablation quadrupole and multiple collector ICPMS analysis: Application to lead isotope analysis. *Analytical Chemistry*, *87*(2), 1152–1157. https://doi.org/10.1021/ac503749k

Iaccarino, S., Montomoli, C., Carosi, R., Massonne, H.-J., Langone, A., & Visonà, D. (2015). Pressure-temperature-time-deformation path of kyanite-bearing migmatitic paragneiss in the Kali Gandaki valley (Central Nepal): Investigation of Late Eocene-Early Oligocene melting processes. *Lithos*, *231*, 103–121. https://doi.org/10.1016/j.lithos.2015.06.005

Iaccarino, S., Montomoli, C., Carosi, R., Montemagni, C., Massonne, H.-J., Langone, A., et al. (2017). Pressure-temperature-deformation-time constraints on the South Tibetan Detachment System in the Garhwal Himalaya (NW India). *Tectonics*, *36*(11), 2281–2304. https://doi.org/10.1002/2017TC004566

Imayama, T., Takeshita, T., Yi, K., Cho, D.-L., Kitajima, K., Tsutsumi, Y., et al. (2012). Two-stage partial melting and contrasting cooling history within the Higher Himalayan Crystalline Sequence in the far-eastern Nepal Himalaya. *Lithos*, *134–135*, 1–22. https://doi.org/10.1016/j.lithos.2011.12.004

Jamieson, R. A., Beaumont, C., Medvedev, S., & Nguyen, M. H. (2004). Crustal channel flows: 2. Numerical models with implications for metamorphism in the Himalayan–Tibetan orogen. *Journal of Geophysical Research*, *109*. B06407. https://doi.org/10.1029/2003JB002811

Kali, E., Leloup, P. H., Arnaud, N., Maheo, G., Liu, D. Y., Boutonnet, E., et al. (2010). Exhumation history of the deepest central Himalayan rocks, Ama Drime range: Key pressure–temperature–deformation–time constraints on orogenic models. *Tectonics*, *29*(2).TC2014. https://doi.org/10.1029/2009TC002551

Kellett, D. A., Cottle, J. M., & Larson, K. P. (2018). *The South Tibetan Detachment System: History, advances, definition and future directions*. In P. J. Treloar, & M. P. Searle (Eds.), Himalayan tectonics: A modern synthesis (Vol. *483*, pp. 377–400). Geological Society Special Publications. https://doi.org/10.1144/SP483.2

Kellett, D. A., Cottle, J. M., & Smit, M. (2014). Eocene deep crust at Ama Drime, Tibet: Early evolution of the Himalayan orogen. *Lithosphere*, *6*(4), 220–229. https://doi.org/10.1130/L350.1

Kellett, D. A., Grujic, D., Coutand, I., Cottle, J., & Mukul, M. (2013). The South Tibetan Detachment System facilitates ultra rapid cooling of granulite-facies rocks in Sikkim Himalaya. *Tectonics*, *32*(2), 252–270. https://doi.org/10.1002/tect.20014

Kellett, D. A., Grujic, D., & Erdmann, S. (2009). Miocene structural reorganization of the South Tibetan detachment, eastern Himalaya: Implications for continental collision. *Lithosphere*, *1*, 259–281. https://doi.org/10.1130/L56.1

Kelsey, D. E., Clark, C., & Hand, M. (2008). Thermobarometric modeling of zircon and monazite growth in melt-bearing systems: Examples using model metapelitic and metapsammitic granulites. *Journal of Metamorphic Geology*, *26*(2), 199–212. https://doi.org/10.1111/j.1525-1314.2007.00757.x

Kelsey, D. E., & Powell, R. (2011). Progress in linking accessory mineral growth and breakdown to major mineral evolution in metamorphic rocks: A thermodynamic approach in the Na_2O-CaO-K_2O-FeO-MgO-Al_2O_3-SiO_2-H_2O-TiO_2-ZrO_2 system. *Journal of Metamorphic Geology*, *29*(1), 151–166. https://doi.org/10.1111/j.1525-1314.2010.00910.x

Knesel, K. M., & Davidson, J. P. (2002). Insights into collisional magmatism from isotopic fingerprints of melting reactions. *Science*, *296*(5576), 2206–2208. https://doi.org/10.1126/science.1070622

Kohn, M. J. (2008). P-T-t data from central Nepal support critical taper and repudiate large-scale channel flow of the Greater Himalayan sequence. *The Geological Society of America Bulletin*, *120*(3–4), 259–273. https://doi.org/10.1130/B26252.1

Kohn, M. J. (2009). Models of garnet differential geochronology. *Geochimica et Cosmochimica Acta*, *73*(1), 170–182. https://doi.org/10.1016/j.gca.2008.10.004

Kohn, M. J. (2014). Himalayan metamorphism and its tectonic implications. *Annual Review of Earth and Planetary Sciences*, *42*(1), 381–419. https://doi.org/10.1146/annurev-earth-060313-055005

Kohn, M. J., & Corrie, S. L. (2011). Preserved Zr-temperatures and U-Pb ages in high-grade metamorphic titanite: Evidence for a static hot channel in the Himalayan orogen. *Earth and Planetary Science Letters*, *311*(1), 136–143. https://doi.org/10.1016/j.epsl.2011.09.008

Kohn, M. J., Corrie, S. L., & Markley, C. (2015). The fall and rise of metamorphic zircon. *American Mineralogist*, *100*(4), 897–908. https://doi.org/10.2138/am-2015-5064

Kohn, M. J., & Kelly, N. M. (2018). Petrology and geochronology of metamorphic zircon. *Microstructural Geochronology: Planetary Records Down to Atom Scale. Geophysical Monograph*, *232*, 35–61. https://doi.org/10.1002/9781119227250.ch2

Kohn, M. J., Wieland, M. S., Parkinson, C. D., & Upreti, B. N. (2004). Miocene faulting at plate tectonic velocity in the Himalaya of central Nepal. *Earth and Planetary Science Letters*, *228*(3–4), 299–310. https://doi.org/10.1016/j.epsl.2004.10.007

Larson, K. P., Ambrose, T. K., Webb, A. A. G., Cottle, J. M., & Shrestha, S. (2015). Reconciling Himalayan midcrustal discontinuities: The Main Central thrust system. *Earth and Planetary Science Letters*, *429*, 139–146. https://doi.org/10.1016/j.epsl.2015.07.070

Larson, K. P., & Cottle, J. M. (2014). Midcrustal discontinuities and the assembly of the Himalayan midcrust. *Tectonics*, *33*(5), 718–740. https://doi.org/10.1002/2013TC003452

Larson, K. P., Gervais, F., & Kellett, D. A. (2013). A P-T-t-D discontinuity in east-central Nepal: Implications for the evolution of the Himalayan mid-crust. *Lithos*, *179*, 275–292. https://doi.org/10.1016/j.lithos.2013.08.012

Lee, J., & Whitehouse, M. J. (2007). Onset of mid-crustal extensional flow in southern Tibet: Evidence from U/Pb zircon ages. *Geology*, *35*(1), 45–48. https://doi.org/10.1130/G22842A.1

Le Fort, P. (1975). Himalayas: The collided range. Present knowledge of the continental arc. *American Journal of Science*, *275*(1), 1–44.

Le Fort, P., Cuney, M., Deniel, C., France-Lanord, C., Sheppard, S. M. F., Upreti, B. N., & Vidal, P. (1987). Crustal generation of the Himalayan leucogranites. *Tectonophysics*, *134*(1), 39–57. https://doi.org/10.1016/0040-1951(87)90248-4

Leloup, P. H., Mahéo, G., Arnaud, N., Kali, E., Boutonnet, E., Liu, D., et al. (2010). The South Tibet detachment shear zone in the Dinggye area. Time constraints on extrusion models of the Himalayas. *Earth and Planetary Science Letters*, *292*(1–2), 1–16. https://doi.org/10.1016/j.epsl.2009.12.035

Li, Q., Zhang, L., Fu, B., Bader, T., & Yu, H. (2019). Petrology and zircon U-Pb dating of well-preserved eclogites from the Thongmön area in central Himalaya and their tectonic implications. *Journal of Metamorphic Geology*, *37*(2), 203–226. https://doi.org/10.1111/jmg.12457

Liu, Y., Gao, S., Hu, Z., Gao, C., Zong, K., & Wang, D. (2010). Continental and oceanic crust recycling-induced melt-peridotite interactions in the trans-North China Orogen: U-Pb dating, Hf isotopes and trace elements in zircons from mantle xenoliths. *Journal of Petrology*, *51*(1–2), 537–571. https://doi.org/10.1093/petrology/egp082

Liu, Z.-C., Wu, F.-Y., Qiu, Z.-L., Wang, J.-G., Liu, X.-C., Ji, W.-Q., & Liu, C.-Z. (2017). Leucogranite geochronological constraints on the termination of the South Tibetan Detachment in eastern Himalaya. *Tectonophysics*, *721*, 106–122. http://dx.doi.org/10.1016/j.tecto.2017.08.019

Lombardo, B., & Rolfo, F. (2000). Two contrasting eclogite types in the Himalayas: Implications for the Himalayan orogeny. *Journal of Geodynamics*, *30*(1–2), 37–60. https://doi.org/10.1016/S0264-3707(99)00026-5

Ludwig, K. R. (2003). *Isoplot/Ex version 3.0*. A geochronological toolkit for Microsoft Excel (Vol. 4, pp. 1–70). Berkeley Geochronology Center Special Publication.

Luvizotto, G. L., & Zack, T. (2009). Nb and Zr behavior in rutile during high-grade metamorphism and retrogression: An example from the ivrea-verbano zone. *Chemical Geology*, *261*(3), 303–317. https://doi.org/10.1016/j.chemgeo.2008.07.023

Mohan, A., Windley, B. F., & Searle, M. P. (1989). Geothermobarometry and development of inverted metamorphism in the Darjeeling-Sikkim region of the eastern Himalayan. *Journal of Metamorphic Geology*, *7*(1), 95–110. https://doi.org/10.1111/j.1525-1314.1989.tb00577.x

Montomoli, C., Carosi, R., & Iaccarino, S. (2015). *Tectonometamorphic discontinuities in the Greater Himalayan Sequence: A local or a regional feature?* In S. Mukherjee, et al. (Eds.), Tectonics of the Himalaya (Vol. *412*, pp. 25–41). Geological Society, Special Publications. http://dx.doi.org/10.1144/SP412.3

Montomoli, C., Iaccarino, S., Carosi, R., Langone, A., & Visonà, D. (2013). Tectonometamorphic discontinuities within the Greater Himalayan Sequence in Western Nepal (Central Himalaya): Insights on the exhumation of crystalline rocks. *Tectonophysics*, *608*, 1349–1370. https://doi.org/10.1016/j.tecto.2013.06.006

Mottram, C. M., Warren, C. J., Regis, D., Roberts, N. M. W., Harris, N. B. W., Argles, T. W., & Parrish, R. R. (2014). Developing an inverted Barrovian sequence: Insights from monazite petrochronology. *Earth and Planetary Science Letters*, *403*, 418–431. https://doi.org/10.1016/j.epsl.2014.07.006

Mukherjee, S. (2015). *A review on out-of-sequence deformation in the Himalaya*. In S. Mukherjee, et al. (Eds.), Tectonics of the Himalaya (Vol. *412*, pp. 67–109). Geological Society, Special Publications. http://dx.doi.org/10.1144/SP412.13

Murphy, M. A., & Mark Harrison, T. (1999). Relationship between leucogranites and the Qomolangma detachment in the Rongbuk Valley, south Tibet. *Geology*, *27*(9), 831–834. https://doi.org/10.1130/0091-7613(1999)027<0831:RBLATQ>2.3.CO;2

Nemchin, A. A., Giannini, L. M., Bodorkos, S., & Oliver, N. H. S. (2001). Ostwald ripening as a possible mechanism for zircon overgrowth formation during anatexis: Theoretical constraints, a numerical model, and its application to pelitic migmatites of the Tickalara Metamorphics, northwestern Australia. *Geochimica et Cosmochimica Acta*, *65*(16). https://doi.org/10.1016/S0016-7037(01)00622-6

Patiño Douce, A. E., & Harris, N. (1998). Experimental constraints on Himalayan anatexis. *Journal of Petrology*, *39*(4), 689–710. https://doi.org/10.1093/petroj/39.4.689

Regis, D., Warren, C. J., Young, D., & Roberts, N. M. W. (2014). Tectono-metamorphic evolution of the Jomolhari massif: Variations in timing of syn-collisional metamorphism across western Bhutan. *Lithos*, *190–191*, 449–466. https://doi.org/10.1016/j.lithos.2014.01.001

Rey, P. F., Teyssier, C., & Whitney, D. L. (2009). Extension rates, crustal melting, and core complex dynamics. *Geology*, *37*(5), 391–394. https://doi.org/10.1130/G25460A.1

Rosenberg, C. L., & Handy, M. R. (2005). Experimental deformation of partially melted granite revisited: Implications for the continental crust. *Journal of Metamorphic Geology*, *23*(1), 19–28. https://doi.org/10.1111/j.1525-1314.2005.00555.x

Rubatto, D. (2017). Zircon: The metamorphic mineral. *Reviews in Mineralogy and Geochemistry*, *83*(1), 261–295. https://doi.org/10.2138/rmg.2017.83.9

Rubatto, D., Chakraborty, S., & Dasgupta, S. (2013). Timescales of crustal melting in the Higher Himalayan Crystallines (Sikkim, Eastern Himalaya) inferred from trace element-constrained monazite and zircon chronology. *Contributions to Mineralogy and Petrology*, *165*(2), 349–372. https://doi.org/10.1007/s00410-012-0812-y

Sachan, H. K., Kohn, M. J., Saxena, A., & Corrie, S. L. (2010). The Malari leucogranite, Garhwal Himalaya, northern India: Chemistry, age, and tectonic implications. *The Geological Society of America Bulletin*, *122*, 1865–1876. https://doi.org/10.1130/B30153.1

Sawyer, E. W., Cesare, B., & Brown, M. (2011). When the continental crust melts. *Elements*, *7*(4), 229–234. https://doi.org/10.2113/gselements.7.4.229

Searle, M. (2013). Crustal melting, ductile flow, and deformation in mountain belts: Cause and effect relationships. *Lithosphere*, *5*(6), 547–554. https://doi.org/10.1130/l006.1

Searle, M. P., Elliott, J. R., Phillips, R. J., & Chung, S.-L. (2011). Crustal-lithospheric structure and continental extrusion of Tibet. *Journal of the Geological Society*, *168*(3), 633–672. http://dx.doi.org/10.1144/0016-76492010-139

Searle, M. P., & Fryer, B. J. (1986). *Garnet, tourmaline and muscovite-bearing leucogranites, gneisses and migmatites from the Higher Himalaya of Zanskar, Lahoul, Kulu and Kashmir*. In: In Coward, M. P., & Ries, A. C. (Eds.), Collision Tectonics, (Vol. 19, pp. 185–201). Special Publication of the Geological Society, London. https://doi.org/10.1144/GSL.SP.1986.019.01.10

Searle, M. P., & Godin, L. (2003). The South Tibetan Detachment and the Manaslu Leucogranite: A structural reinterpretation and restoration of the Annapurna-Manaslu Himalaya, Nepal. *The Journal of Geology*, *111*(5), 505–523. https://doi.org/10.1086/376763

Searle, M. P., Parrish, R. R., Hodges, K. V., Hurford, A., Ayres, M. W., & Whitehouse, M. J. (1997). Shisha pangma leucogranite, south Tibetan Himalaya: Field relations, geochemistry, age, origin, and emplacement. *The Journal of Geology*, *105*(3), 295–318. https://doi.org/10.1086/515924

Searle, M. P., Simpson, R. L., Law, R. D., Parrish, R. R., & Waters, D. J. (2003). The structural geometry, metamorphic and magmatic evolution of the Everest massif, High Himalaya of Nepal-South Tibet. *Journal of the Geological Society*, *160*(3), 345–366. http://dx.doi.org/10.1144/0016-764902-126

Searle, M. P., & Szulc, A. G. (2005). Channel flow and ductile extrusion of the high Himalayan slab-the Kangchenjunga-Darjeeling profile, Sikkim Himalaya. *Journal of Asian Earth Sciences*, *25*(1), 173–185. https://doi.org/10.1016/j.jseaes.2004.03.004

Sláma, J., Košler, J., Condon, D. J., Crowley, J. L., Gerdes, A., Hanchar, J. M., et al. (2008). Plešovice zircon—A new natural reference material for U-Pb and Hf isotopic microanalysis. *Chemical Geology*, *249*(1), 1–35. https://doi.org/10.1016/j.chemgeo.2007.11.005

Sorcar, N., Hoppe, U., Dasgupta, S., & Chakraborty, S. (2014). High-temperature cooling histories of migmatites from the High Himalayan Crystallines in Sikkim, India: Rapid cooling unrelated to exhumation? *Contributions to Mineralogy and Petrology*, *167*(2), 957. https://doi.org/10.1007/s00410-013-0957-3

Spear, F. S., & Pyle, J. M. (2002). Apatite, monazite, and xenotime in metamorphic rocks. *Reviews in Mineralogy and Geochemistry*, *48*(1), 293–335. https://doi.org/10.2138/rmg.2002.48.7

Spear, F. S., & Pyle, J. M. (2010). Theoretical modeling of monazite growth in a low-Ca metapelite. *Chemical Geology*, *273*(1–2), 111–119. https://doi.org/10.1016/j.chemgeo.2010.02.016

Tian, Z., Zhang, Z., & Dong, X. (2016). Metamorphism of high-P metagreywacke from the Eastern Himalayan syntaxis: Phase equilibria and P-T path. *Journal of Metamorphic Geology*, *34*(7), 697–718. https://doi.org/10.1111/jmg.12205

Viskupic, K., Hodges, K. V., & Bowring, S. A. (2005). Timescales of melt generation and the thermal evolution of the Himalayan metamorphic core, Everest region, eastern Nepal. *Contributions to Mineralogy and Petrology*, *149*(1), 1–21. https://doi.org/10.1007/s00410-004-0628-5

Visonà, D., & Lombardo, B. (2002). Two-mica and tourmaline leucogranites from the Everest-Makalu region (Nepal-Tibet). Himalayan leucogranite genesis by isobaric heating? *Lithos*, *62*(3–4), 125–150. https://doi.org/10.1016/S0024-4937(02)00112-3

Walters, J. B., & Kohn, M. J. (2017). Protracted thrusting followed by late rapid cooling of the Greater Himalayan Sequence, Annapurna Himalaya, central Nepal: Insights from titanite petrochronology. *Journal of Metamorphic Geology*, *35*(8), 897–917. https://doi.org/10.1111/jmg.12260

Wang, J.-M., Rubatto, D., & Zhang, J.-J. (2015). Timing of partial melting and cooling across the Greater Himalayan Crystalline Complex (Nyalam, central Himalaya): In-sequence thrusting and its implications. *Journal of Petrology*, *56*(9), 1677–1702. https://doi.org/10.1093/petrology/egv050

Wang, J.-M., Zhang, J.-J., Liu, K., Zhang, B., Wang, X.-X., Rai, S., & Scheltens, M. (2016). Spatial and temporal evolution of tectonometamorphic discontinuities in the central Himalaya: Constraints from P-T paths and geochronology. *Tectonophysics*, *679*, 41–60. https://doi.org/10.1016/j.tecto.2016.04.035

Wang, J. M., Zhang, J. J., & Wang, X. X. (2013). Structural kinematics, metamorphic P-T profiles and zircon geochronology across the Greater Himalayan Crystalline Complex in south-central Tibet: Implication for a revised channel flow. *Journal of Metamorphic Geology*, *31*(6), 607–628. https://doi.org/10.1111/jmg.12036

Wang, Y., Zhang, L., Zhang, J., & Wei, C. (2017). The youngest eclogite in central Himalaya: P-T path, U-Pb zircon age and its tectonic implication. *Gondwana Research*, *41*, 188–206. https://doi.org/10.1016/j.gr.2015.10.013

Warren, C. J., Beaumont, C., & Jamieson, R. A. (2008). Formation and exhumation of ultra-high-pressure rocks during continental collision: Role of detachment in the subduction channel. *Geochemistry, Geophysics, Geosystems*, *9*. https://doi.org/10.1029/2010TC002738

Warren, C. J., Grujic, D., Kellett, D. A., Cottle, J., Jamieson, R. A., & Ghalley, K. S. (2011). Probing the depths of the India-Asia collision: U-Th-Pb monazite chronology of granulites from NW Bhutan. *Tectonics*, *30*(2). https://doi.org/10.1029/2010TC002738

Warren, C. J., Singh, A. K., Roberts, N. M. W., Regis, D., Halton, A. M., & Singh, R. B. (2014). Timing and conditions of peak metamorphism and cooling across the Zimithang Thrust, Arunachal Pradesh, India. *Lithos*, *200–201*, 94–110. https://doi.org/10.1016/j.lithos.2014.04.005

Weinberg, R. F. (2016). Himalayan leucogranites and migmatites: Nature, timing and duration of anatexis. *Journal of Metamorphic Geology*, *34*(8), 821–843. https://doi.org/10.1111/jmg.12204

Wu, F. Y., Liu, Z. C., Liu, X. C., & Ji, W. Q. (2015). Himalayan leucogranite: Petrogenesis and implications to orogenesis and plateau uplift. *Acta Petrologica Sinica*, *31*, 1–36. Retrieved from http://en.cnki.com.cn/Article_en/CJFDTotal-YSXB201501001.htm. (in Chinese with English abstract)

Yakymchuk, C., & Brown, M. (2014). Behavior of zircon and monazite during crustal melting. *Journal of the Geological Society*, *171*(4), 465–479. http://dx.doi.org/10.1144/jgs2013-115

Yakymchuk, C., & Brown, M. (2019). Divergent behavior of Th and U during anatexis: Implications for the thermal evolution of orogenic crust. *Journal of Metamorphic Geology*, *37*, 899–916. https://doi.org/10.1111/jmg.12469

Yakymchuk, C., Clark, C., & White, R. W. (2017). Phase relations, reaction sequences and petrochronology. *Reviews in Mineralogy and Geochemistry*, *83*(1), 13–53. https://doi.org/10.2138/rmg.2017.83.2

Yakymchuk, C., Kirkland, C. L., & Clark, C. (2018). Th/U ratios in metamorphic zircon. *Journal of Metamorphic Geology*, *36*, 715–737. https://doi.org/10.1111/jmg.12307

Yin, A. (2006). Cenozoic tectonic evolution of the Himalayan orogen as constrained by along-strike variation of structural geometry, exhumation history, and foreland sedimentation. *Earth-Science Reviews*, *76*(1), 1–131. https://doi.org/10.1016/j.earscirev.2005.05.004

Yin, A., & Harrison, T. M. (2000). Geologic evolution of the Himalayan-Tibetan orogen. *Annual Review of Earth and Planetary Sciences*, *28*(1), 211–280. https://doi.org/10.1146/annurev.earth.28.1.211

Zeng, L., Gao, L.-E., Dong, C., & Tang, S. (2012). High-pressure melting of metapelite and the formation of Ca-rich granitic melts in the Namche Barwa Massif, southern Tibet. *Gondwana Research*, *21*(1), 138–151. https://doi.org/10.1016/jgr.2011.07.023

Zeng, L., Gao, L.-E., Xie, K., & Liu-Zeng, J. (2011). Mid-Eocene high Sr/Y granites in the Northern Himalayan Gneiss Domes: Melting thickened lower continental crust. *Earth and Planetary Science Letters*, *303*(3–4), 251–266. https://doi.org/10.1016/j.epsl.2011.01.005

Zhang, H., Harris, N., Parrish, R., Kelley, S., Zhang, L., Rogers, N., et al. (2004). Causes and consequences of protracted melting of the mid-crust exposed in the North Himalayan antiform. *Earth and Planetary Science Letters*, *228*(1), 195–212. https://doi.org/10.1016/j.epsl.2004.09.031

Zhang, Z., Ding, H., Dong, X., Tian, Z., Kang, D., Mu, H., et al. (2018). High-temperature metamorphism, anataxis and tectonic evolution of a mafic granulite from the eastern Himalayan orogen. *Journal of Earth Sciences*, *29*(5), 1010–1025. https://doi.org/10.1007/S12583-018-0852-Y

Zhang, Z., Xiang, H., Dong, X., Ding, H., & He, Z. (2015). Long-lived high-temperature granulite-facies metamorphism in the Eastern Himalayan orogen, south Tibet. *Lithos*, *212–215*, 1–15. https://doi.org/10.1016/j.lithos.2014.10.009

Zhang, Z., Xiang, H., Dong, X., Li, W., Ding, H., Gou, Z., & Tian, Z. (2017). Oligocene HP metamorphism and anatexis of the Higher Himalayan Crystalline Sequence in Yadong region, east-central Himalaya. *Gondwana Research*, *41*, 173–187. https://doi.org/10.1016/j.gr.2015.03.002

Zhang, Z. M., Xiang, H., Ding, H. X., Dong, X., Gou, Z. B., Tian, Z. L., & Santosh, M. (2017). Miocene orbicular diorite in east-central Himalaya: Anatexis, melt mixing, and fractional crystallization of the Greater Himalayan Sequence. *The Geological Society of America Bulletin*, *129*(7–8), 869–885. https://doi.org/10.1130/B31586.1

Zhang, Z. M., Zhao, G. C., Wang, J. L., Dong, X., & Liou, J. G. (2010). Two stages of granulite facies metamorphism in the eastern Himalayan syntaxis, south Tibet: Petrology, zircon geochronology and implications for the subduction of Neo-Tethys and the Indian continent beneath Asia. *Journal of Metamorphic Geology*, *28*(7), 719–733. https://doi.org/10.1111/j.1525-1314.2010.00885.x

Zong, K., Klemd, R., Yuan, Y., He, Z., Guo, J., Shi, X., et al. (2017). The assembly of Rodinia: The correlation of early Neoproterozoic (ca. 900 Ma) high-grade metamorphism and continental arc formation in the southern Beishan Orogen, southern Central Asian Orogenic Belt (CAOB). *Precambrian Research*, *290*, 32–48. https://doi.org/10.1016/j.precamres.2016.12.010